Wiley Series on Mass Spectrometry

Dominic M. Desiderio, Joseph A. Loo, and Nico M. M. Nibbering, Series Editors

# Cluster Secondary Ion Mass Spectrometry

## *Principles and Applications*

*Edited by Christine M. Mahoney*

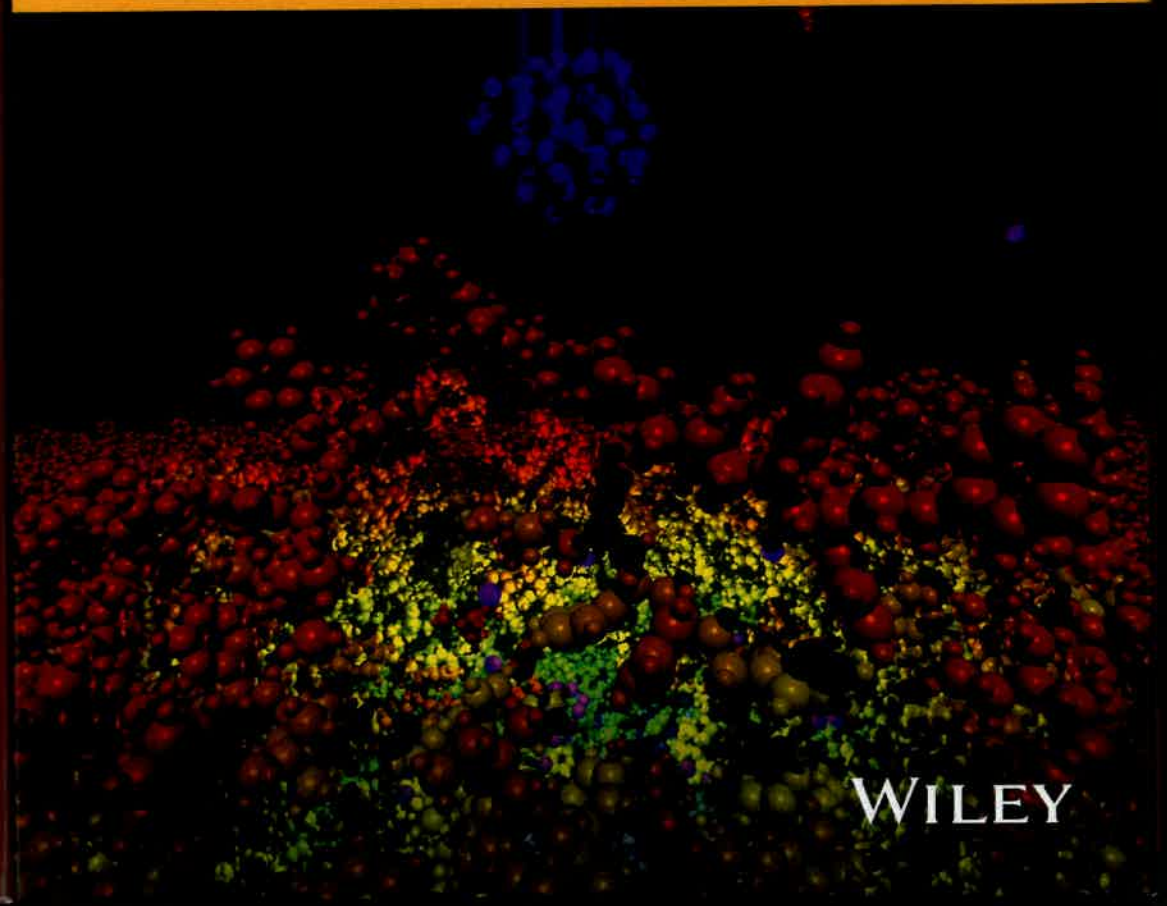

WILEY

Published by John Wiley & Sons, Inc., Hoboken, New Jersey
Published simultaneously in Canada



***Library of Congress Cataloging-in-Publication Data:***

Mahoney, Christine M., 1975-
Cluster secondary ion mass spectrometry : principles and applications / Christine M. Mahoney.
pages cm
Includes bibliographical references and index.
ISBN 978-0-470-88605-2 (hardback)
1. Secondary ion mass spectrometry. I. Title.
QD96.S43M34 2013
543'.65–dc23

2012045181

Printed in Singapore

10 9 8 7 6 5 4 3 2 1

CHAPTER 6

# THREE-DIMENSIONAL IMAGING WITH CLUSTER ION BEAMS

*Andreas Wucher, Gregory L. Fisher, and Christine M. Mahoney*

## 6.1 INTRODUCTION

One of the most challenging tasks in surface and thin-film technology is the ability to perform three-dimensional chemical characterization of surface and subsurface structures with high spatial and depth resolution. Such information is, for instance, ultimately needed in semiconductor technology, where devices are highly integrated and stacked with vertical dimensions approaching the nanometer scale. While this was, in the past, mainly done with inorganic materials, designs are now shifting to organic devices, where it is important to analyze the *molecular* structure rather than just the elemental composition. Another demand is triggered by the immensely growing field of biological applications, where it becomes important to localize specific molecules within samples such as tissue and single cells.

In principle, 3D chemical characterization requires an imaging analysis technique that allows both lateral (i.e., parallel to the surface) and vertical (i.e., perpendicular to the surface) resolution on the nanometer scale. Lateral resolution can be obtained by microscope or microprobe imaging techniques which may either employ stigmatic imaging of species carrying the spectroscopic information or by raster scanning a finely focused excitation probe in order to obtain chemically specific information. Vertical resolution, on the other hand, requires the applied imaging technique to be surface sensitive, that is, to probe chemical information only from the uppermost layers of an investigated sample. Useful analytical techniques are therefore restricted to methods such as electron spectroscopy or surface mass spectrometry, delivering chemical information with nanometer scale

*Cluster Secondary Ion Mass Spectrometry: Principles and Applications*, First Edition.
Edited by Christine M. Mahoney.

information depth. However, only surface mass spectrometric-based methods have the ability to obtain molecular information without the need of specific tags.

Surface mass spectrometry utilizes a primary excitation beam to energize the surface, thereby generating surface-specific particles that are then analyzed with respect to their mass-to-charge ratio. Possible primary excitation mechanisms include laser desorption (laser ablation mass microanalysis, LAMMA; laser ionization microanalysis, LIMA; laser desorption and ionization, LDI; matrix-assisted laser desorption/ionization, MALDI), ion sputtering (secondary ion mass spectrometry/secondary neutral mass spectrometry, SIMS/SNMS), electron-stimulated desorption (ESD) or bombardment of the surface with energetic macrodroplets (desorption electrospray ionization, DESI). Among these, only laser desorption and ion sputtering allow for high resolution lateral imaging with molecule-specific information. However, while the laser beam focus is restricted by the diffraction limit, limiting the maximum spatial resolution to the micrometer scale, ion beams can, in principle, be focused down to a spot size of several nanometers,[1] allowing for molecular imaging with spatial resolutions in the nanoscale range. Moreover, the information depth of laser desorption (micrometer range) is much larger than that of ion sputtering (~1 nm), leaving SIMS (and SNMS) as the only viable method for high resolution three-dimensional chemical imaging on the nanometer scale.

A prominent strategy for 3D surface and thin-film characterization is to combine laterally resolved surface analysis with layer-by-layer sample erosion, thereby gradually exposing the subsurface material to a method for surface-sensitive chemical analysis. Among the various possible approaches for controlled erosion, sputter depth profiling has evolved as one of the most versatile tools to obtain chemical information as a function of depth below the initial surface. Here, the solid surface is bombarded by an energetic ion beam, thereby removing surface material because of ion sputtering. Combined with imaging surface analysis, this strategy, although destructive, allows one to reconstruct the three-dimensional structure of the investigated sample by means of a tomography approach, that is, stacking successive 2D slices as illustrated in Figure 6.1a.

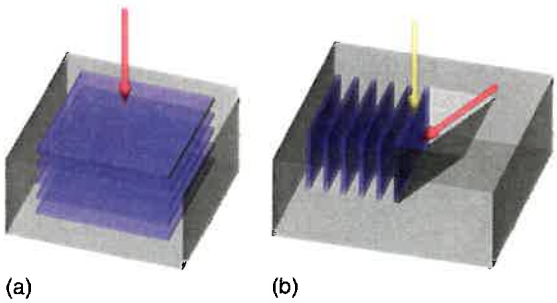


Figure 6.1 Schematic view of (a) 3D sputter depth profiling and (b) 3D focused ion beam (FIB) tomography. Red arrows indicate the direction of analysis. The yellow arrow in (b) indicates the FIB milling direction. The blue planes represent the successive image stacks.

In principle, every imaging method can be used to analyze the momentarily exposed surface, as long as it is sufficiently surface sensitive and delivers chemistry-specific information at a meaningful level. Mass spectrometry techniques such as SIMS or SNMS are capable of providing molecule-specific information about the surface chemistry and may therefore directly be used for the analysis of molecular samples, provided the chemical integrity of the surface can be preserved under high fluence ion bombardment as is necessary for sputter erosion. While this was originally deemed impossible when atomic projectile ions were more conventionally used for sputtering, the advent of cluster ion beams has dramatically changed this picture. As shown in Chapter 5, molecular sputter depth profiling using cluster projectiles such as $SF_5^+$, $C_{60}^+$, or $Ar_n^+$ (with $n$ up to several thousand) is now regarded as routine, with an achievable depth resolution of the order of 10 nm or below.

Although there have been quite a few successful demonstrations of 3D SIMS analysis using this approach, there are many potential artifacts that can arise in the data because of inaccurate assumptions (e.g., nonlinear sputter rates and topographic artifacts). Moreover, a fundamental problem in nanoscale 3D imaging, particularly of molecular systems, is related to detection sensitivity. Typical number densities of such systems are of the order of several molecules per cubic nanometer of sample volume. If one would set out to measure the chemical composition of such a sample with a spatial resolution of $10 \times 10 \times 10$ nm$^3$, such a "voxel" would only contain a few thousand (matrix) molecules that are available for analysis. If the analyte molecule of interest is not the matrix itself but only present in minor concentration, this number further reduces accordingly. The probability of a sputtered molecule leaving the surface as an intact, unfragmented molecular secondary ion is typically rather small (of the order of $10^{-5} \cdots 10^{-3}$), and even for characteristic fragments this number is not significantly larger. This means that (much) less than one single ion would, on average, be detectable from each voxel in a SIMS experiment. Therefore, one needs to find a useful spatial resolution that can be defined by the condition that at least one ion should be detectable from a voxel. From the above estimates, it is clear that this may require the voxel volume to be increased by orders of magnitude, which can be accomplished by sacrifices either in lateral (parallel to the surface) or in-depth (along the surface normal) resolution.

This chapter outlines the considerations that must be taken into account when obtaining and analyzing 3D molecular imaging data. A series of guidelines for beam conditions during sputter depth profiling are described, as well as important data analysis considerations. It is shown that 3D imaging should always be correlated with sample topography in order to display true 3D representations of the data. Furthermore, correction factors accounting for differential sputtering, initial surface topography, and low data density are introduced. Finally, although the primary focus of this chapter will be on sputter depth profiling with cluster ion beams, other means of obtaining in-depth information from soft samples will also be discussed (e.g., Focused Ion Beam SIMS (FIB-SIMS) and physical cross sectioning methods). Overall it is expected that this chapter will serve as a set of guidelines for 3D organic analysis using SIMS.

## 6.2 GENERAL STRATEGIES

There are several approaches to obtaining 3D molecular information as a function of depth using SIMS or SNMS, based both on physical cross sectioning and ion bombardment methods. Each of these approaches will now be discussed in turn.

### 6.2.1 Three-Dimensional Sputter Depth Profiling

The standard strategy of 3D sputter depth profiling involves acquiring a stack of mass spectrometric images that are separated by intermediate sputter erosion cycles. One example of experimental data acquired using this strategy was shown in Chapter 5 (Fig. 5.7). Other examples of data acquired in this manner are shown in Figures 6.2, through 6.6, and Figure 6.8. In fact, most of the data published to date have been obtained in this way. Mass spectral data are usually acquired using time-of-flight (ToF) spectrometry in order to allow parallel detection of all masses and avoid any restriction of the acquired mass range. During the acquisition of an image, the surface is kept in a "static" mode where the applied projectile ion fluence is low enough to prevent damage or erosion of more than a small fraction (typically less than 1%) of a monolayer. As an important feature of this strategy, data acquisition and sputter erosion are decoupled and can, in principle, be performed using different ion beams using, for instance, the high lateral resolution of a liquid metal ion gun (LMIG) beam for image acquisition along with the low damage cross section of a cluster ion beam for sputter erosion. The projectile ion beam used for ToF data acquisition is operated in a pulsed mode and digitally rastered across the desired analysis field-of-view.

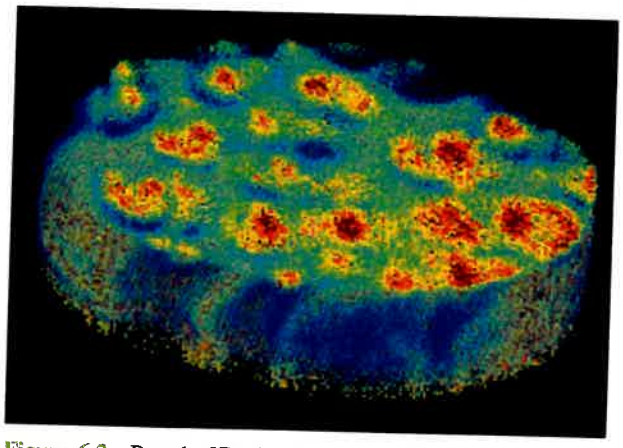

**Figure 6.2** Pseudo-3D visualization of SIMS data at *m/z* 152 acquired on an acetaminophen-doped PLA polymer film using a 250 μm field-of-view. Sputter erosion and data acquisition was performed using a 10 keV $SF_5^+$ cluster ion beam, and image acquisition was performed in microscope mode. Reproduced from Gillen et al.,[23] with permission from Elsevier.

C


**Figure 6.3**
(PLGA, gre
different elu
cluster ion l
from Fisher


Duri
mode and
applying a
method of
inorganic s
resolution,
cussed in
have been
via elemer
elemental
optimizing
will restric
analysis, w
Fron
revert to a
ing applica

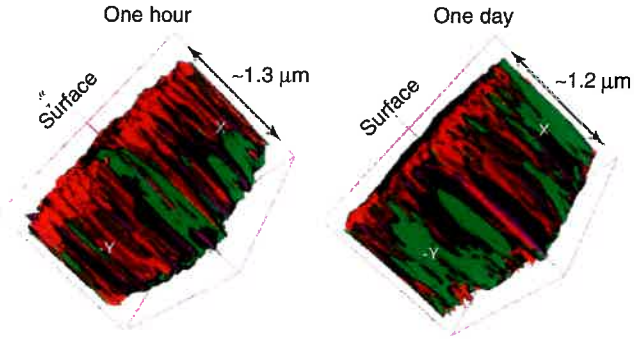


**Figure 6.3** Pseudo-3D visualization of ToF-SIMS data at *m/z* 84 (sirolimus, red), *m/z* 56 (PLGA, green) and *m/z* 23 (Na, purple) acquired on a coronary stent coating for two different elution times (as indicated). Sputter erosion was performed using a 20 keV $C_{60}^+$ cluster ion beam and images were acquired using a 30 keV $Au^+$ ion beam. Reproduced from Fisher et al.,[24] with permission from ACS Publications.

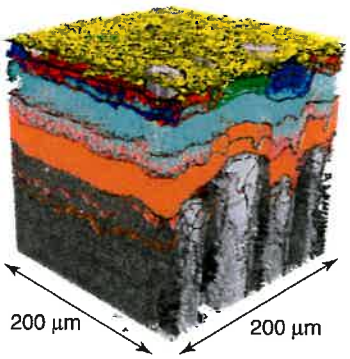


**Figure 6.4** Pseudo-3D visualization of ToF-SIMS data of various molecular ions at *m/z* 500–850 acquired on an OLED display structure. Sputter erosion was performed using a 5 keV $Ar_{1700}^+$ cluster ion beam and images were acquired using a 25 keV $Bi_3^+$ beam. Data courtesy of ION-TOF GmbH, Germany.

During an erosion cycle, the sputtering ion beam is operated in a continuous mode and rastered over the desired erosion area for a preselected amount of time, applying a certain ion fluence per sputtering cycle. It should be noted that this method of depth profiling has a more mature standing for elemental analysis of inorganic samples,[2,3] where issues such as the relation between useful lateral image resolution, detection sensitivity, and statistical signal noise have already been discussed in great detail.[1,4–7] There are also a number of studies where molecules have been localized using this method, for instance, imaging inside single cells via elemental and isotopic tagging of the molecule of interest.[8–14] In a few cases, elemental imaging using cluster ion beams was attempted with the intention of optimizing the depth resolution as compared to atomic projectile ions.[15–23] We will restrict the discussions here to the more recent applications of *molecular* 3D analysis, which has only been made possible by the use of cluster ion beams.

From the body of data that has been published during the past decade, we revert to a few recent examples illustrating the application. One of the more promising applications of the cluster ion beam is for imaging and depth profiling in drug

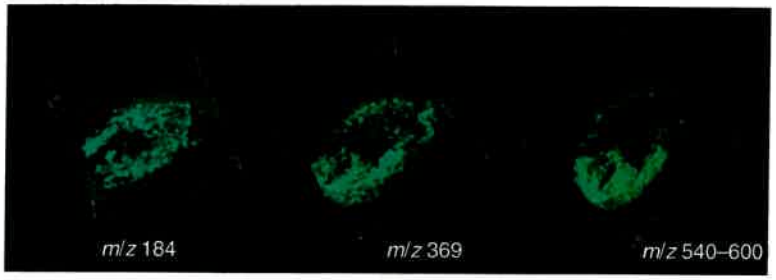


**Figure 6.5** Pseudo-3D visualization of ToF-SIMS data at *m/z* 184 (phosphocholine head group), *m/z* 369 (cholesterol), and *m/z* 540–600 (assigned to phosphatidylcholine lipids) acquired on a frog's egg cell (*Xenopus laevis* oocyte). Image acquisition and sputter erosion were performed using a 40 keV $C_{60}^+$ cluster ion beam. Reproduced from Fletcher et al.,[70] with permission from Springer.

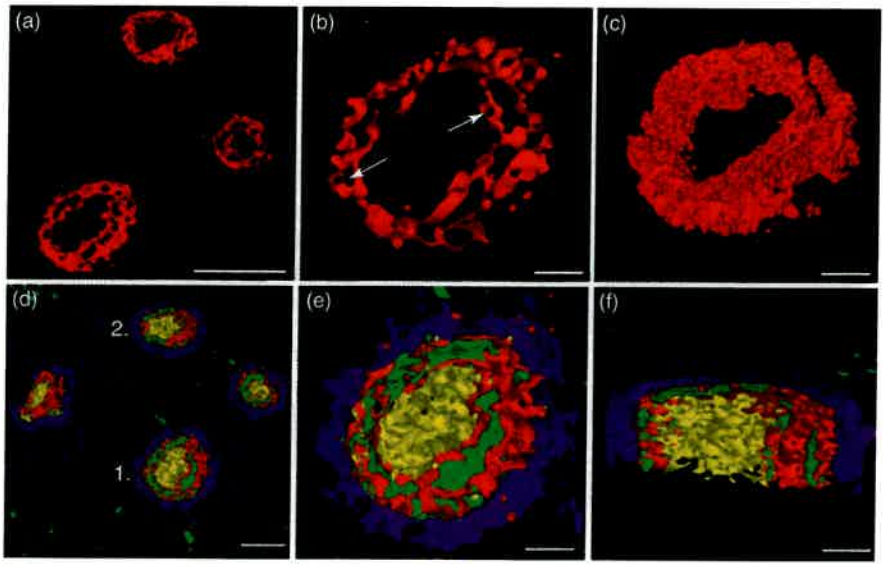


**Figure 6.6** Pseudo-3D visualization of ToF-SIMS data at *m/z* 23 (Na, blue), *m/z* 39 (K, green), *m/z* 184 (phosphocholine head group, red), and *m/z* 86 (phosphocholine fragment, yellow) acquired on single thyroid tumor cells. Sputter erosion was performed using a 10 keV $C_{60}^+$ cluster ion beam and images were acquired using a 25 keV $Bi_3^+$ beam. Reproduced from Nygren et al.,[74] with permission from Wiley.

delivery systems. An example of this was given in Chapter 5 for protein delivery systems (Fig. 5.7). Figure 6.2 shows an earlier example with the analysis of a poly(lactic acid) (PLA) film doped with 20% (weight) of a drug (acetaminophen).[23] Sputter erosion and data acquisition were performed using a 10 keV $SF_5^+$ ion beam and images of the drug-specific molecular ion signal at *m/z* 152 were acquired in microscope mode (see section 6.3.1 for definition of microscope mode). It is clearly evident that the drug distribution is highly inhomogeneous.

Figure 6.3 shows another example of image depth profiling of a drug-eluting coronary stent coating that is composed of 25% (w/w) of a drug (sirolimus) in a poly(lactic-*co*-glycolic acid) (PLGA) matrix.[24] The data were taken in a dual beam configuration using a 30 keV $Au^+$ ion beam for image acquisition and a 20 keV $C_{60}^+$ ion beam for sputter erosion. The figure displays a 3D visualization of the resulting image stack showing characteristic molecular fragment ion signals representative of the drug (red) and the PLGA matrix (green) along with that of sodium (purple) after two different elution times. The study shows that the spatial distribution of the drug is related to the elution rate.

With the more recent advent of the gas cluster ion beam source (GCIB), the ability of cluster SIMS for depth profiling in organic electronics has improved dramatically, opening up new doors for characterization of photovoltaics, organic light emitting diodes (OLED), and other organic-based electronics devices. Figure 6.4 depicts an example of 3D analysis in an OLED structure as part of a modern computer display.[25] As is typical for integrated circuits, the sample is highly stacked and structured both in lateral and vertical dimensions. Using a rare gas cluster ion beam (5 keV $Ar_{1700}^+$) for sputter erosion and a 25 keV $Bi_3^+$ LMIG ion beam for data acquisition, one can easily identify the different regions using molecule-specific SIMS signals; a feat previously unattainable using any other cluster beam.

One of the most important impacts of the cluster source however, is the ability to obtain 3D molecular information from biological systems on the single cell level. Figure 6.5 shows the first published example of three-dimensional molecular analysis in a biological single cell system.[26] A relatively large (about 1 mm diameter) frog's egg cell (*Xenopus laevis* oocyte) was freeze dried and a 3D depth profile of the entire cell was performed using a 40 keV $C_{60}^+$ ion beam both for sputter erosion and data acquisition. The important result of this study was that (i) it is possible to erode several micrometers deep into the cell material and (ii) the spatial distribution of molecular ions specific to certain cell components can clearly be discerned.

This pioneering work was later followed by 3D profiles of other biological cells. For example, Figure 6.6 depicts data acquired on freeze-fractured and freeze-dried anaplastic thyroid carcinoma cells.[27] The displayed 3D visualization of the resulting data set clearly shows the structure of a single cell, featuring an enrichment of sodium (blue) from the dry culture medium around the cell periphery, followed by a correlated appearance of potassium (green), and the phosphocholine head group (a characteristic fragment of phospholipids at *m/z* 184, red), which are taken to be representative for the cell membrane. In the inner region of the cells, an enhanced signal at *m/z* 86 is found, which is assumed to represent a characteristic fragment of the phosphocholine head group in phospholipids.

In a different instrumental approach, a continuous (DC) ion beam is used for data acquisition and sputter erosion at the same time.[28,29] The beam is rastered across the desired erosion area and mass spectral data are acquired using either a quadrupole mass filter, a pulsed ToF spectrometer, or a combination of both.[28,29] Images are acquired by registering the mass spectrometric signal as a function of the momentary beam position on the sample, which can be varied by either scanning the beam[29] or translating the sample.[28] This way, each measured data point represents

an integral over a voxel determined by the lateral beam spot size and the depth eroded during the dwell time of the beam on each pixel. Using the shortest feasible dwell time of about 10 µs along with a cluster ion beam current of 1 nA into a spot size of 1 µm, a typical sputter yield volume of the order of 100 $nm^3$/impact would correspond to a voxel depth of the order of 3 nm eroded per acquired image. The great advantage of this technique is that practically all sputtered material is used to generate an image, thereby greatly enhancing the detection sensitivity as compared to the conventional alternating cycle method. Furthermore, the analysis times are significantly decreased when employing continuous beams. Again, the lateral voxel (pixel) dimension is restricted by the spot size of the eroding cluster ion beam, which presently limits the achievable lateral resolution to about 1 µm.

A prominent example of a data set acquired using this method is shown in Figure 6.7. The data were taken on formalin-fixed benign hyperplasia prostate cells.[30] The displayed 3D visualization using isosurface rendering along with cross-sectional images clearly shows a localization of the adenine molecular ion signal (*m/z* 136, left panel) representing the DNA in the center of the cells, while the phosphocholine head group fragment signal (*m/z* 184, right panel) representing the lipid cell membrane appears to be localized at the circumference of each cell.

The above examples clearly illustrate that meaningful 3D imaging analysis of complex molecular systems can be performed if cluster ion beams are used for sputter erosion. In order to construct a 3D visualization of the acquired data set, the measured ToF-SIMS images were in all cases simply stacked in the vertical direction with arbitrary equidistant spacing. It should be stressed that such a visualization relies on three implicit assumptions:

1. each image represents a flat slice across the analyzed sample;
2. the original sample surface is flat;
3. there is a linear relation between applied ion fluence and eroded depth, which is the same everywhere in the analyzed volume.

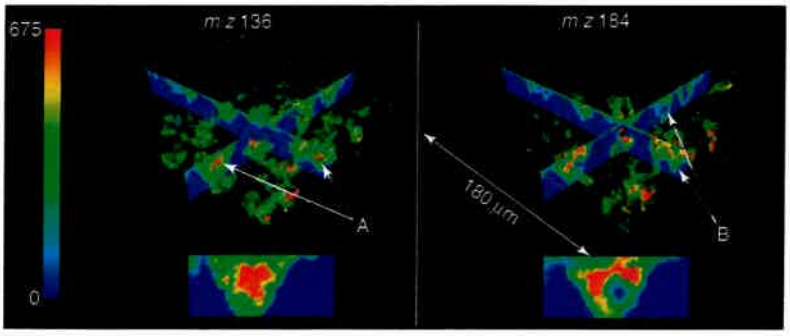


**Figure 6.7** Pseudo-3D visualization of ToF-SIMS data at *m/z* 136 (the protonated molecular ion from adenine) and *m/z* 184 (the phosphocholine lipid head group) acquired on benign prostatic hyperplasia cells. Sputter erosion and image acquisition was performed using a 40 keV $C_{60}^+$ cluster ion beam operated in DC mode. Reproduced from Fletcher et al.,[30] with permission from ACS Publications.

In cases where one (or more) of these assumptions is violated, the resulting visualization may greatly deviate from the true three-dimensional sample structure. Examples for such conditions will be shown below. While visualizations of this kind may be extremely valuable to identify the *presence* of different chemical regions in the analyzed sample, they may at the same time be greatly misleading as to the *exact location* of these regions as well as their *spatial dimensions*. In order to illustrate this statement, we refer to an example of a specially prepared test structure consisting of a 300 nm peptide-doped trehalose film deposited on a silicon substrate that was prestructured using a 15 keV $Ga^+$ focused ion beam (FIB) in order to generate significant surface topographical features. This sample was then analyzed by an imaging sputter depth profile using a 20 keV $C_{60}^+$ ion beam for erosion and data acquisition. The simple 3D visualization of the resulting data set is depicted in Figure 6.8, where an overlay of ToF-SIMS signals representative for the molecular overlayer (the peptide molecular ion at *m/z* 425, blue), the FIB projectile material (Ga at *m/z* 69, red), and the silicon substrate (Si at *m/z* 28, green) is shown. The image reveals that $Ga^+$ bombardment of the molecular film

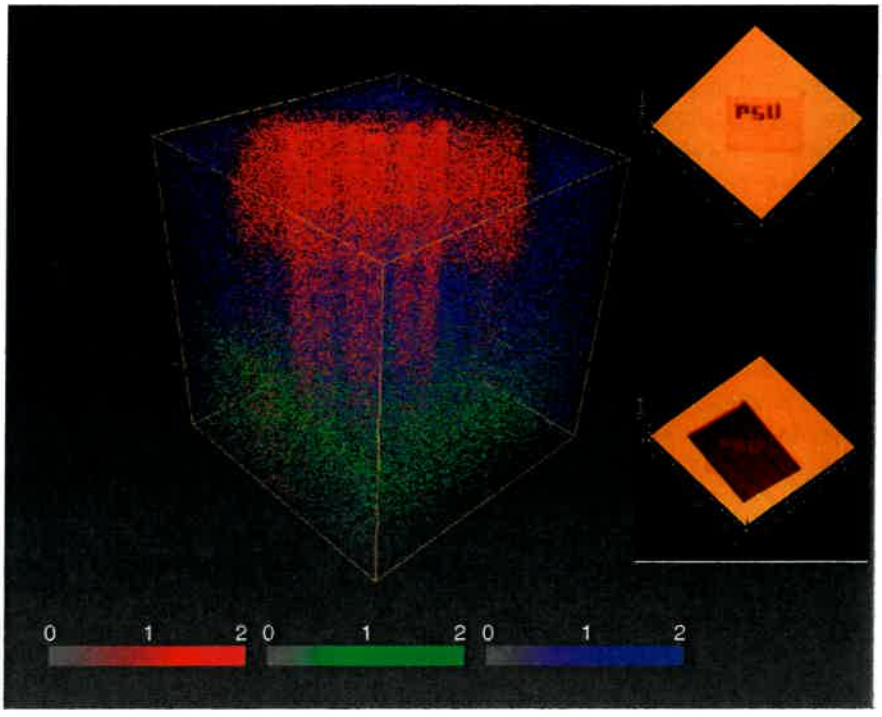


**Figure 6.8** Pseudo-3D visualization of ToF-SIMS data at *m/z* 425 (molecular ion of GGYR peptide, blue), *m/z* 69 (Ga, red), and *m/z* 28 (Si, green) acquired on a 300 nm trehalose film deposited on Si and prestructured using a 15 keV $Ga^+$ FIB beam. Image acquisition and sputter erosion were performed using a 20 keV $C_{60}^+$ cluster ion beam. Insert: AFM images of the surface taken before and after depth profile analysis. Recreated from Wucher et al.,[58] with permission from ACS publications.

generates a gallium-implanted subsurface region, where the molecular integrity of the sample is practically destroyed. However, the acquired SIMS data do not contain any information regarding the topography of the surface analyzed in each individual ToF-SIMS image. As a consequence, the visualization cannot deliver information about the thickness of the damaged layer, not even of the undamaged parts of the film. In the same way, the data presented in Figure 6.2 and Figure 6.3 reveal an inhomogeneous drug distribution within the analyzed volume; however, the true location of the drug-enriched regions cannot be discerned because the depth information is only qualitative.

Similarly, Figure 6.4 shows that there are different structures stacked in the analyzed volume, but the data deliver no information as to the thickness or depth of the individual films, so it remains unclear which structure is neighbored to which. This information, however, is vital to understanding the electrical functionality of the device. Finally, the data shown in Figure 6.5 reveal the presence of specific molecules such as cholesterol in the interior of the analyzed cells, but it does not provide information on where exactly these molecules are located. For that reason, we will, in the following, call such a simple image stacking procedure a *pseudo-3D* visualization of a measured data set.

In principle, the ion fluence applied between the acquisition of subsequent images must be converted into eroded depth. As will be discussed below, the assumption of a constant erosion rate across the entire sample volume is not always justified, so that this conversion will in general be nonlinear and require a careful depth scale calibration. The data processing from a pseudo-3D visualization as shown in Figures 6.2 through 6.8 to a true three-dimensional representation of the sample chemistry therefore ultimately requires the combination of 3D imaging with topography data taken on the investigated sample before, during, and after the sputter depth profile analysis. Possible methods to obtain such data are stylus profilometry, atomic force microscopy (AFM), or optical interferometry. Conceptually, the best strategy would be to acquire such data *in situ* during the acquisition of the sputter depth profile. While such instrumentation is not currently available, one can at the very least measure the surface topography *ex situ* before and after the depth profile using, for instance, AFM. Examples for such a protocol will be shown in the following section.

### 6.2.2 Wedge Beveling

Another strategy used to obtain 3D information is by creating a bevel cut across the sample volume of interest and performing an image analysis of the resulting cross section. The bevel cut can be generated either mechanically,[31] via chemical etching,[32] or via ion sputtering using a controlled lateral variation of the applied ion fluence.[33] The latter technique was introduced many years ago as a means of depth scale calibration during inorganic sputter depth profiling.[34]

An example for such an analysis of a molecular film has recently been published by Mao et al.,[35,36] who investigated a system of organic delta layers (Irganox 3114) embedded into an Irganox 1010 matrix. Figure 6.9 shows a ToF-SIMS image

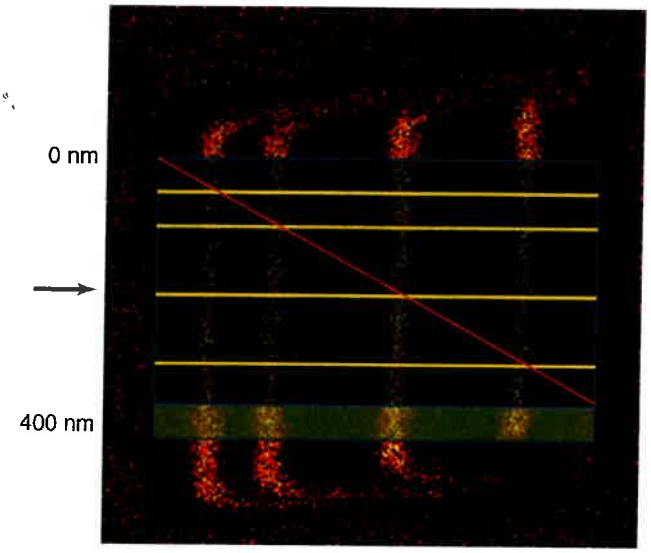


**Figure 6.9** ToF-SIMS image of a wedge bevel crater eroded into Irganox 1010 doped with four delta layers of Irganox 3114. The image shows the intensity of the *m/z* 42 molecular fragment signal representing the delta layers with the arrow indicating the impact direction of the $C_{60}$ ion beam. Insert: schematic side view of wedge (red line) across Irganox 1010 matrix (blue) and Irganox 3114 layers (yellow) down to silicon substrate (green). Recreated from Mao et al.,[36] with permission from ACS Publications.

of a wedge crater eroded into the sample using a 40 keV $C_{60}^+$ cluster ion beam impinging under 71° with respect to the surface normal. As pointed out in the original publication, it is important that the sputter erosion was performed with the sample at cryogenic temperature. The image was acquired using the same $C_{60}^+$ ion beam, but now impinging under 40° with respect to the surface normal. The shape of the eroded crater was measured with AFM and is schematically depicted in the insert as a red line, spanning a range from zero depth (the original surface) on the left hand side to erosion of the entire molecular overlayer down to the silicon substrate on the right hand side. The position of the four delta layers are indicated as yellow lines. It is evident that the displayed SIMS image of the *m/z* 42 fragment signal of Irganox 3114 exhibits pronounced maxima right where the bevel cut crosses the delta layers, thereby clearly demonstrating that it is possible to localize the embedded Irganox 3114 molecules with a nanometer precision and a depth resolution of about 10 nm.

### 6.2.3 Physical Cross Sectioning

An alternative approach, one that avoids the issues inherent during sputtering, is to use secondary methods to slice the sample into thin sections, analyze each of the individual slices in succession, and subsequently stack the images for 3D data representation. Such processes have already proven to be successful for analysis

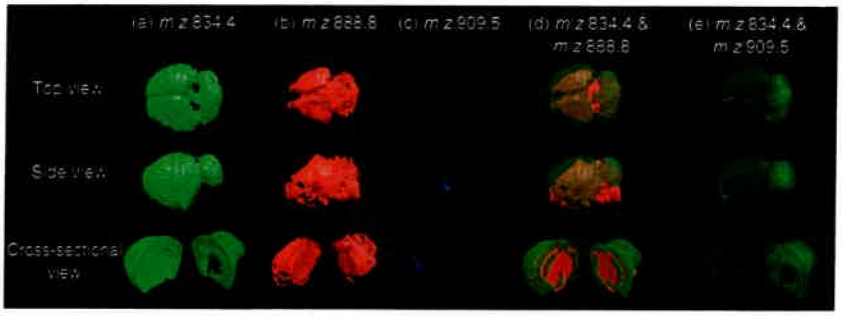


**Figure 6.10** Three-dimensional models of the mouse brain by DESI-MS. The signals imaged are characteristic of phosphatidylserines (PS), phosphatidylinositols (PI), and sulfatides (ST) where PS 18:0/22:6 is the major lipid found in the gray matter and ST 24:1 is the major lipid found in the white matter. Top, side, and cross-sectional views are shown for the 3D reconstruction of the distribution of (a) PS 18:0/22:6 in green, (b) ST 24:1 in red, and (c) PI 18:0/22:6 in blue. The same views are shown for the transparent overlaid distributions of the lipids, (d) PS18:0/22:6 and ST24:1 and (e) PS 18:0/22:6 and PI 18:0/22:6. Reproduced from Eberlin et al.,[38] with permission from Wiley.

and 3D imaging with MALDI[37] and DESI.[38] An example is depicted in Figure 6.10 that shows the 3D molecular composition of lipids in a mouse brain, obtained using DESI to characterize a series of 20 µm cryosectioned slices.

Another means of obtaining 3D information without the difficulties of sputtering artifacts is by creating a bevel cut such as was described earlier, except by physically cutting the sample using a method such as ultralow angle microtomy (ULAM). An example is given by Hinder et al.,[39] where the authors used ULAM to cut into a sample of acrylic paint. The slice was created at an angle and subsequently imaged using SIMS in order to obtain in-depth information from the sample.

Figure 6.11 shows the resulting SIMS images of the various components in the paint coating, acquired from a beveled crater bottom. The negative ion images

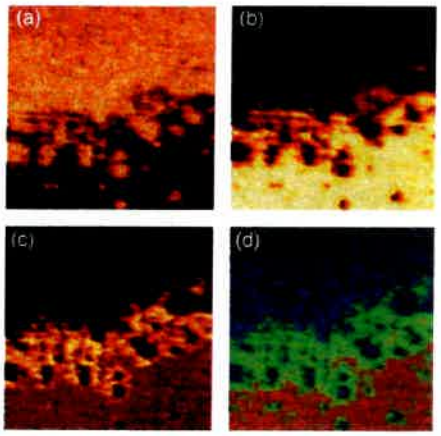


**Figure 6.11** Negative ion ToF-SIMS images (500 µm × 500 µm) of a buried polymer/polymer interface exposed by ultralow angle microtomy. (a) *m/z* 66, polyurethane (PU) primer (located 20 µm below surface), (b) *m/z* 19, poly(vinylidene difluoride) (PVDF) coating, (c) *m/z* 85, acrylic copolymers, and (d) overlay of PU (blue), PVDF (red), and acrylics (green). Findings confirm that the acrylic copolymers segregate to the topcoat/primer interface where they enhance the adhesive properties. Recreated from Hinder et al.,[39] with permission from Wiley.

displayed in the figure were acquired using a $Au_3^+$ cluster source and show intense molecular and atomic ion images from three different polymeric components in the film: (i) the polyurethane (PU) primer coat located ~20 μm below the surface (*m/z* 66), (ii) the poly(vinylidene difluoride) (PVDF) topcoat (*m/z* 19), and (iii) acrylic PMMA/poly(ethyl methacrylate) (PEMA) copolymers that are shown in the figure to segregate the interface region (*m/z* 85).[39] The data are summarized in an overlay of the three regions, Fig. 6.11(d), created subsequently by the authors of this chapter. This result helped to understand the mechanisms of adhesion in this particular coating, whereby the acrylic copolymer promotes adhesion between the primer and topcoat by segregating the interface. More important, however, is that this method does not have the problems inherent with sputtering and can be useful for analysis of thicker coatings.

### 6.2.4 FIB-ToF Tomography

A conceptually different approach to obtain 3D chemical information involves a combination of FIB etching and imaging ToF mass spectrometry. A FIB is a highly focused $Ga^+$ beam that can be used to etch small features into a surface (e.g., lithography), and/or create cross sections and lift-out sections in materials for subsequent analysis with other technologies. For example, FIB is often used in conjunction with secondary electron microscopy (FIB-SEM) to obtain 3D structural information.[40–42] FIB-SEM may also be used in conjunction with energy dispersive X-ray spectroscopy (EDS) capabilities or with wavelength dispersive X-ray spectroscopy (WDS) to obtain elemental information in three dimensions.[41] While the results are promising for 3D analysis, however, there are several limitations to these analytical methods which include low sensitivity, poor spectroscopic resolution, limited chemical information, and no information concerning molecular or structural chemistry—limitations that are readily overcome by employing a SIMS analysis approach.

FIB has been used in conjunction with a quadrupole-based secondary ion mass spectrometer to obtain 3D elemental maps of inorganic samples, in a process referred to as *FIB-SIMS*.[43,44] More recently, an *in situ* FIB option in conjunction with ToF-SIMS imaging mass spectrometry for 3D characterization has been developed—an analytical approach that is called *FIB-ToF*. In this approach, the FIB beam is first used to mill away the sample material around the volume of interest. As indicated in Figure 6.1b, this will lead to "vertical" cutting planes that represent cross sections of the analyzed volume in the direction parallel to the FIB beam. These cross sections can then be imaged using ToF SIMS.

An example of such a strategy is shown in Figures 6.12 and 6.13. A specimen of sintered CuW composite* was used to demonstrate the efficacy of the FIB-ToF approach for 3D characterization wherein successive FIB milling and ToF-SIMS acquisition cycles were employed to image a 10 μm deep volume at a 20 μm × 20 μm analytical field-of-view. Before depth profile analysis, a FIB cross section

*Dr. Noel Smith of Oregon Physics and Sherbrooke Metals is acknowledged for providing the CuW composite material.

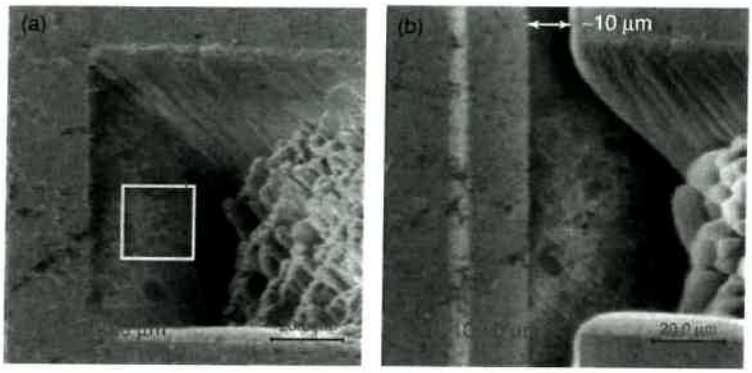


**Figure 6.12** Ion-induced secondary electron (SE) images from the CuW composite. (a) An SE image of the initial FIB-milled cross section. The approximate location of the 20 μm × 20 μm analytical field-of-view is indicated. (b) An SE image of the imaged surface following the FIB-ToF tomography. The measured milled depth is approximately 10 μm. Each image is a 100 μm × 100 μm field-of-view (scale bar is 20 μm). The depth of the cross section at the vertical back wall is approximately 50 μm. Data courtesy of Physical Electronics (2010).[45]

was milled into the central region of the sample. The initial cross section for the CuW composite is depicted in Figure 6.12a that shows a secondary electron (SE) image of the initial cross section crater created by the FIB, where the direction of the FIB ion beam cut was 45° with respect to the surface normal, and the LMIG analysis was performed at 90° with respect to the FIB cut, such that the vertical back wall of the FIB crater was in the direct line-of-sight of the LMIG (refer to Fig. 6.1b).

This image reveals the slope of the cross section crater and the slight curtaining[46] as a result of the FIB milling. Additionally, the SE image reveals a large degree of topography at the crater bottom. This topography is the result of differential sputtering and is produced at least in part, when certain components of a composite matrix are sputtered more readily than others; in the present case, the tungsten sputters more readily than does the copper. Since in this design, the analyst is characterizing the vertical back wall of the FIB cross section, the slight topography and/or curtaining does not interfere with analysis as it would during SIMS depth profiling, and a nominally smooth surface is revealed after each slice.

An SE image was also obtained following 20 FIB line cuts and ToF-SIMS acquisition cycles, and is shown in Figure 6.12b where the measured depth of milling in the direction of the line cuts parallel to the surface is 10 μm. The image reveals that after 20 individual line cuts, the back wall of the crater exposed to the LMIG remains sharp, the W grains remain well-defined, and the curtaining has not worsened. It is also observed that the sputtered material from the line cuts has partially deposited onto the crater bottom and side walls.

The 20 individual raw data stream files from the ToF-SIMS analyses of the FIB-sectioned CuW composite were compiled, or concatenated, into a single raw file for the purposes of extracting depth profiles and 3D images, where the resulting

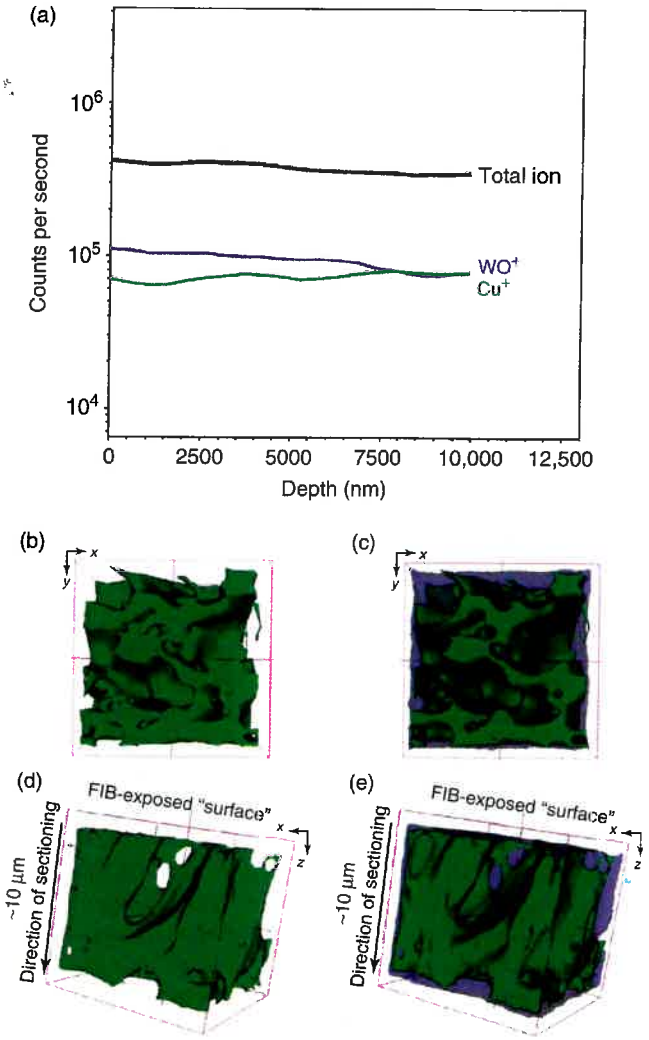


**Figure 6.13** (a) FIB-ToF depth profile of the $Cu^+$, $WO^+$, and total ion signals that were extracted following concatenation of the 20 individual raw data stream files. The depth scale is based on the total measured depth of the FIB line cuts. For each secondary ion species that is monitored, each data point of the depth profile is a sum of the counts of that species across the entire raster frame, that is 20 μm × 20 μm. (b–e) 3D isosurface models of $Cu^+$ (green) and $WO^+$ (blue; reduced opacity) that were generated from the concatenated raw data stream file. (b) Surface view of the $Cu^+$ isosurface model; (c) surface view of the $Cu^+$ and $WO^+$ isosurface overlay; (d) side view of the $Cu^+$ isosurface model; (e) side view of the $Cu^+$ and $WO^+$ isosurface overlay. In each 3D image, the total volume is 20 μm × 20 μm × 10 μm. Data courtesy of Physical Electronics (2010).[45]

depth profiles of $Cu^+$ and $WO^+$ are rendered in Figure 6.13a. For comparison, the total ion profile is also shown. What is noteworthy is that other than minor undulation of the $Cu^+$ and $WO^+$ signals, the profiles are quite unremarkable. There are no pronounced fluctuations of either $Cu^+$ and $WO^+$. The profiles of $W^+$ and $WO_2^+$ show the same trend but have reduced signals.

The corresponding three-dimensional distribution of $Cu^+$ and $WO^+$ data are provided in Figure 6.13b–e where the $Cu^+$ (green) and the $WO^+$ (blue) isosurfaces[47,48] are presented in an overlay. The intensity thresholds of the $Cu^+$ and $WO^+$ 3D images were adjusted to produce isosurface models such that nominally pure copper phases and all tungsten oxide grains are visualized. These areas of copper are discernible in Figure 6.13b and 6.13d where, in both images, the cavities occupied by tungsten oxide are evident. However, there are large quantities of copper that exist in mixed phases with tungsten oxide. The corresponding overlay images in Figure 6.13c and 6.13e, wherein the opacity of the $WO^+$ isosurface has been reduced to expose the internal structure, reveal the 3D distribution of both copper and tungsten oxide. Using the isosurface overlays, the full 3D distribution of each imaged component may be readily observed and fully explored. This level of 3D materials characterization would not be possible via conventional ToF-SIMS depth profiling with a low voltage sputter ion beam because of the artifacts produced as a result of differential sputtering.

Of course, a difficulty of ion beam milling in general is the resulting damage that is imparted to organic molecules. A paramount concern regarding the efficacy of 3D imaging by FIB-ToF tomography is whether the characteristic organic chemistry can be observed, or recovered, following FIB sectioning. Preliminary data indicate that following FIB milling, characteristic and molecular organic signals may be recovered for ToF-SIMS imaging. Before image acquisition, the cross-sectional surface must be subjected to a "polishing" step in order to remove the damaged layer produced by the lateral straggling of the cutting FIB beam. For molecular analysis, a suitable cluster ion beam ($C_{60}^+$ or $Ar_n^+$) can be used for that purpose in order to remove the chemical damage produced by the high energy $Ga^+$ ions. Then, image acquisition can be performed in a static mode. This is demonstrated in Figure 6.14 that presents SE images of a 20 μm PLGA sphere doped with cocaine at a mass fraction of 10%.[†] The sphere was then cross-sectioned by FIB, where the top portion of the sphere was removed (Fig. 6.14a). The FIB milling was performed such that the straggle, or residual damage layer of graphitic carbon produced by FIB milling, is on the order of 10 nm thickness.[49] A 20 keV $C_{60}^+$ ToF-SIMS depth profile was performed on the cross-sectional surface with the objective of determining whether the characteristic molecular and fragment ion signals of the PLGA matrix and the cocaine dopant could be recovered. The molecular formula of cocaine is $C_{17}H_{21}NO_4$ with a molecular weight of 303.35 g/mol; the molecular ion $[M + H]^+$ is observed at 304.36 *m/z*. However, the initial ToF-SIMS analysis revealed little but carbon on the as-received surface.

[†]Dr. Christopher Szakal, Matt Staymates, and Keana Scott of NIST are acknowledged for their efforts in producing and FIB sectioning of the polymer sphere specimens.


Figure 6.1
sphere cor
of the sph
100 μm. (
field-of-vi

The
depth sca
polymers
region of
gerated b
adventitic
condition
The
taminatio
sputterin
cocaine a
lateral di
at-depth
The 2D i
molecule
sample (
image). T
demonstr
the spher
the sourc
to arise
topograp
As
FIB-cutti
ume and
Figure 6
"depth"

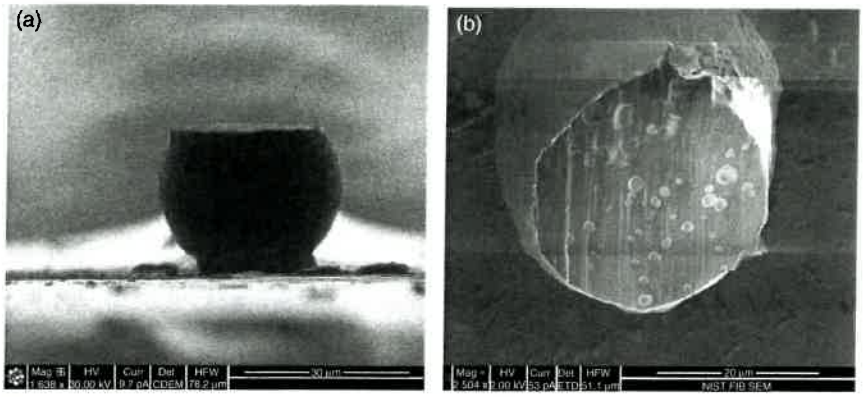


**Figure 6.14** Secondary electron (SE) images of a FIB-milled, 20 μm diameter polymer sphere comprised of cocaine (10 wt.%) in PLGA. (a) Side view showing that the surface of the sphere has been removed by FIB milling. The field-of-view is approximately 100 μm. (b) Surface view revealing the morphology of the FIB-milled sphere. The field-of-view is approximately 40 μm. Data courtesy of Physical Electronics (2010).[45]

The depth profile of the FIB-milled sphere is rendered in Figure 6.15a. The depth scale has been approximated based on the sputter rates of bulk and spin cast polymers including PLGA (~15.1 $nm^3/C_{60}^+$).[47,50] Therefore, the depth scale in the region of the surface that is comprised primarily of FIB-damaged polymer is exaggerated by approximately 1 order of magnitude. Additionally, there is likely some adventitious surface contamination from transportation of the sample at ambient conditions between FIB milling and ToF-SIMS analysis.

The depth profile analysis reveals that after the adventitious surface contamination and the FIB-induced damage layers have been removed via $C_{60}^+$ ion sputtering, the characteristic ion signals of PLGA and the molecular ion signal of cocaine are dramatically improved. At each analytical cycle of the depth profile, the lateral distribution of each chemical constituent is imaged, and these 2D images-at-depth may be extracted from the raw data file at any specified depth interval. The 2D images-at-depth in Figure 6.15b reveal the lateral distribution of cocaine molecules, that is $[M + H]^+$ at *m/z* 304.36, from the surface of the as-received sample (top image) and at a profiled depth of 1 μm from the surface (bottom image). The cocaine molecular ion image acquired before and after $C_{60}$ sputtering demonstrates that the cocaine signal arises only from the FIB-milled surface of the sphere after the FIB-induced surface damage has been removed. At this time, the source of the heterogeneity in the cocaine signal is unknown, but is presumed to arise via phase segregation after production of the spheres, as opposed to a topography affect.

As explained above, three-dimensional analysis is achieved by subsequently FIB-cutting more and more material away from the edge of the analyzed volume and stacking the resulting cross-sectional images as was indicated earlier in Figure 6.1b. Note that, as vertical cross sections are being imaged, the resulting "depth" resolution in the direction perpendicular to the original sample surface is

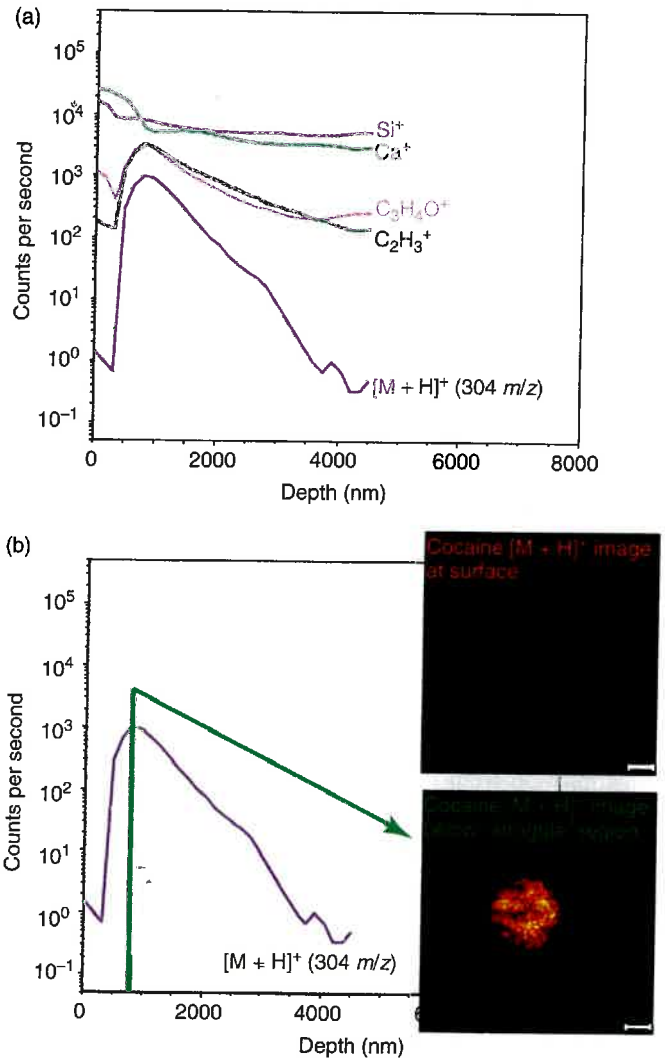


**Figure 6.15** (a) ToF-SIMS depth profiles of $Si^+$, $Ca^+$, the nonspecific $C_2H_3^+$ organic fragment, the characteristic $C_3H_4O^+$ fragment of PLGA, and the cocaine $[M + H]^+$ molecular ion. The depth scale is based on the steady-state sputter rate of PLGA and similar polymers. (b) ToF-SIMS depth profile of the cocaine $[M + H]^+$ molecular ion with corresponding molecular images: The top image shows the secondary ion image of cocaine $[M + H]^+$ at the surface of the as-received FIB-milled polymer sphere, and the bottom image shows the secondary ion image of cocaine $[M + H]^+$ extracted from the raw data file at the depth of maximum cocaine signal. In each image, the scale bar is 10 μm. Data courtesy of Physical Electronics (2010).[45]

determined by the lateral resolution of the imaging technique rather than by typical sputter depth profiling characteristics of the cutting beam. For cluster beams such as $C_{60}^+$ or $Ar_n^+$, this limits the "depth" resolution to about 1 μm. If higher image resolution is required, the system must be equipped with a third ion gun providing, for instance, an LMIG for image acquisition. In this case, "depth" resolution of the order of 100 nm might be achievable. Note that this value is much larger than that obtained by ordinary sputter depth profiling (~10 nm). Moreover, it should be noted that the spatial resolution in the stacking direction (perpendicular to the cutting beam) is *not* equivalent to the spot size of the cutting beam, but rather is determined by the thickness of the laterally damaged layer. Experience reveals that this will limit the achievable resolution to values of the order of 10–30 nm.

## 6.3 IMPORTANT CONSIDERATIONS FOR ACCURATE 3D REPRESENTATION OF DATA

### 6.3.1 Beam Rastering Techniques

Imaging surface analysis can, in principle, be done in two different ways. In the *microscope* mode, a large surface area is being excited at the same time and the resulting signal is detected using a stigmatic imaging technique. Instrumentation for the operation of SIMS in this mode is available using either electromagnetic mass filtering or ToF mass spectrometry, delivering a lateral resolution on the micrometer scale. In the *microprobe* mode, the ion beam used for image acquisition is focused and digitally rastered across the desired analysis field-of-view where the resulting signal is detected as a function of the momentary beam position. The lateral resolution achievable in this mode is largely defined by the spot size of the excitation beam.

When beam rastering is used, the ion beam used for sample erosion must be focused (or defocused) and rastered such that there is a laterally homogenous ion flux density across the desired erosion area. In principle, rastering can be performed either by scanning the beam in analog mode or by stepping the beam across a digital raster pattern. While the former has often been used in conventional sputter depth profiling where the erosion area is generally chosen to be much larger than the "gated" analysis area, it is of limited use for 3D depth profiling experiments, as it is extremely hard to achieve a laterally homogenous current density profile across the entire eroded crater. Therefore, digital rastering schemes should be employed where the beam is stepped across a freely selectable pixel sequence within the desired erosion area. The beam itself can, in principle, be operated in a continuous mode, but in this case extreme care must be taken that the computer controlling the experiment does not perform any other task except stepping the beam and acquiring the data.[‡] Otherwise, the beam might spend ill-defined times on subsequent pixels, possibly resulting in an extremely inhomogeneous erosion profile. It is therefore

[‡]Note that this is impossible to assure if the experiment is controlled by software running under a multitasking operation system.

$C_2H_3^+$ organic
: $[M + H]^+$
f PLGA and
nolecular ion with
ı image of cocaine
ınd the bottom
ɔm the raw data
r is 10 μm. Data

better to operate the beam in a pulsed mode in order to fix the dwell time on each pixel. As commonly known from FIB technology,[51–51] this time should be chosen as small as possible to minimize material redeposition across the eroded volume (Fig. 6.12).

Moreover, the raster scanned area during erosion should not be much larger than the analyzed area when applying a certain projectile ion fluence (as is commonly done in conventional sputter depth profiling), but rather be matched to the image acquisition area when acquiring a molecular 3D profile. Multiple raster frames using short pixel dwell time should be preferred as compared to a single raster with long dwell time when applying the selected ion fluence during an erosion cycle in order to minimize material redeposition effects. Note that the conditions described above for 3D analysis of organic samples, specifically in reference to equal erosion and image areas, is different from what is typically done during 2D sputter depth profiling. When acquiring sputter depth profiles, the selected or gated analysis area is usually much smaller than the erosion area so as to avoid crater edge effects. In 3D profiling this is not necessary because the gating area for depth profiles extracted from the acquired data set can always be selected and optimized in retrospect (see following paragraphs).

Finally, the focal width of the eroding beam must be matched to the lateral pixel size. If the beam spot size is much larger than the pixel dimension, the applied fluence will not match the value calculated from the selected rastering area, and large edge effects will distort the profile at the boundary of the eroded crater. If, on the other hand, the spot size is small compared to the pixel dimension, a corrugated fluence profile is generated which results in the erosion of an egg carton-shaped crater bottom. It is evident that such an erosion profile will spoil the depth resolution and must therefore be avoided. Optimum conditions are established when the beam spot size (full width at half maximum, FWHM) matches the pixel dimension. In cases where it cannot be avoided to work with a too tightly focused beam (for instance, if an extremely large erosion area is needed), the raster pattern should be dithered between subsequent frames. For that purpose, a pixel is divided into subpixels, and the entire raster pattern is shifted across these subpixels between subsequent multiple raster frames.

### 6.3.2 Geometry Effects

As a first step in 3D depth profiling, it is necessary to define an appropriate coordinate system. For the case of an ideally flat surface, this is a straightforward task leading to lateral coordinates ($x$, $y$) in the direction parallel to the surface and a vertical (depth or height) coordinate $z$ along the surface normal. In cases where the analyzed surface exhibits any significant topography, however, this choice is not trivial and one would define these coordinates relative to the *average* surface. Sputter erosion, on the other hand, always proceeds along the *local* surface normal that does not necessarily coincide with the overall depth coordinate, $z$. Moreover, the sputter yield (i.e., the average number of atoms or molecule equivalents removed per projectile impact) is known to depend on the projectile impact angle with respect to the surface normal, which may vary locally for a heavily corrugated

surface. For the description of erosion phenomena, it is convenient to define the sputter yield in terms of the *yield volume*, $Y_v$, that is, the average sample volume removed per projectile impact. The (local) erosion rate is then given by

$$\frac{dz'}{df} = Y_v \text{ or } \frac{dz'}{dt} = j_p \cdot Y_v \tag{6.1}$$

where $z'$ denotes the depth eroded along the local surface normal, $f$ is the projectile ion fluence (or dose), and $j_p = df/dt$ is the projectile ion flux density. Note that $j_p$ can vary locally, for instance, because of an inhomogeneous current density profile of the rastered ion beam. The erosion rate along the depth coordinate $z$ is then given as

$$\frac{dz}{df} = \frac{dz'}{df} \cdot \cos\vartheta \tag{6.2}$$

with $\vartheta$ describing the local surface tilt, that is, the angle between the local surface normal and the $z$-axis.

In many cases of practical interest, the tilt angles $\vartheta$ are very small and can be neglected. In this context, it should be noted that surface topography images usually show a largely magnified vertical scale. For instance, in the example depicted in Figure 6.8, the maximum slope within the trench walls is of the order of 75 nm/μm, which translates to a maximum $\vartheta$ of 4°. In these cases, the erosion rate can safely be approximated by Equation 6.1. There are, however, other cases one could imagine where this approximation fails. An example of such a scenario would be the erosion of a polymer bead as depicted in Figure 6.14, which might, for instance, serve as a prototype of a single cell. If such an object is to be analyzed by 3D sputter depth profiling, one must take the surface angle into account both via the sputter yield and the correction of Equation 6.2. Using the known impact angle dependence of the sputter yield, one can simulate the erosion profile for such an object by numerical integration of Equation 6.1. An example of this is shown in Figure 6.16, where the shape of an originally hemi-elliptical object on a flat surface is calculated for equidistant ion fluence steps using the angular sputter yield variation as measured by Kozole et al.[54] for a cholesterol film bombarded with a 40 keV $C_{60}^+$ ion beam. As displayed in Figure 6.16a, the experimental yield data were fitted to a suitable functional form and cut off by a quadratic function for impact angles above 75°.[§] The bottom panel shows the resulting height profile of the object at different projectile ion fluences, where the length units of the axes are arbitrary as long as both are the same. The direction of projectile impact is indicated by the arrow. The evolution of the shape of the bombarded object at various stages of the erosion is evident. At points where the incident ion beam strikes tangential to the surface (or, which are shadowed from the impinging ion beam), erosion is not possible and the erosion rate is zero. As a consequence, topographical features develop which may even give rise to instabilities, leading to a macroscopic roughening of the surface. It is obvious that under such circumstances the assumption of a constant and homogeneous erosion rate (which implicitly forms the basis of pseudo-3D

[§]The sputter yield must necessarily go to zero for impact angles approaching 90°.

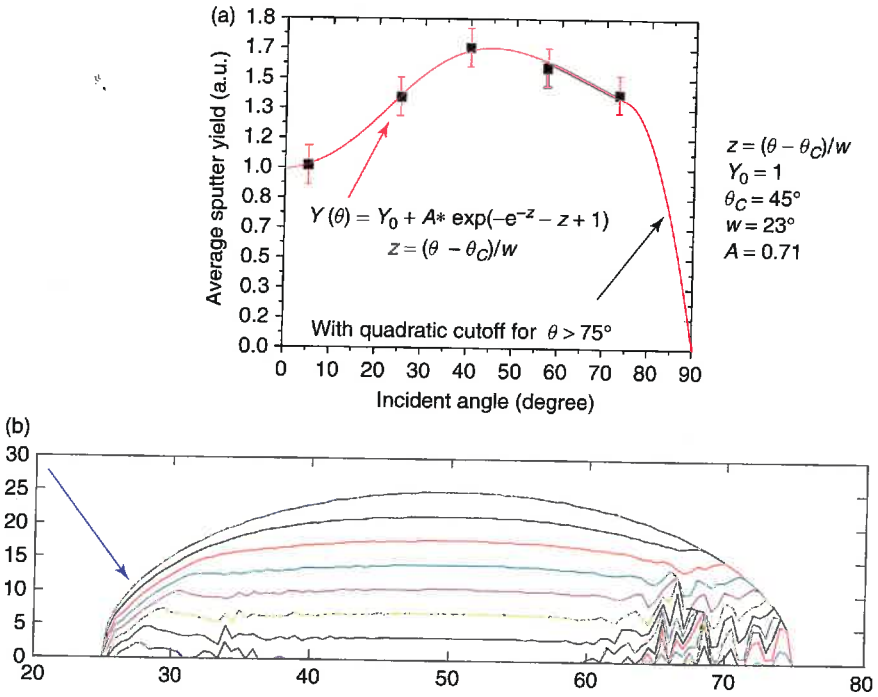


Figure 6.16 Cross-sectional erosion profile of an elliptical object bombarded with a parallel cluster ion beam under 45° impact with respect to the substrate surface as indicated by the blue arrow in panel (b). The different colors refer to equidistant steps of the projectile ion fluence, with the blue line depicting the original shape of the object at zero fluence. The numbers at the axes can be interpreted in any length unit as long as both are identical. The data were calculated using the impact angle dependence of the sputter yield depicted in panel (a) (data points measured for cholesterol under $C_{60}^+$ bombardment[54] and fitted by the indicated functional form).

image stacking) must be largely misleading. It should also be noted that sample rotation during ion bombardment may reduce but not completely mitigate these effects.

### 6.3.3 Depth Scale Calibration

Although the pseudo-3D representation depicted in Figures 6.3 through 6.6 provides some qualitative insight, more steps are required to achieve a true 3D representation of the analyzed sample volume. The crucial goal is to evaluate the $z$-coordinate at which a particular voxel $(i,j,k)$ corresponding to a pixel $(j,k)$ in an acquired image number $(i)$ was actually located in the sample. Three factors determine the height (depth) of a voxel. First, the topography of the original surface before sputter depth profiling must be known. In the following examples described, the topography was determined from AFM images of the surface measured before the depth profile analysis. Second, the ion fluence applied during the depth profiling experiment

must be converted into eroded depth. In general, this depth scale calibration will be nonlinear because the erosion rate can vary significantly between different vertical layers. Moreover, as outlined earlier, erosion rates can, in principle, also vary between different lateral areas of the sample, thus making the depth progression between subsequently acquired images pixel-dependent.

As a starting point to address the depth scale calibration, it is necessary to register topography images obtained before and after (and ideally also during) the depth profile analysis in a pixel-by-pixel manner with the acquired chemical images. Since orientation and displacement can be different for all these data sets, at least two marker points must exist at the surface that can be unambiguously identified in all images. Note that these markers must be located outside the eroded crater area because otherwise they will be destroyed during the depth profile acquisition. If the sample does not *a priori* contain suitable features, they can be imprinted using a focused ion beam. As an important step, the topography images must be cropped and converted to the same pixel resolution as the chemical images. If image area and erosion area were chosen to be the same during the depth profile analysis, this task is straightforward as the erosion area is clearly visible as the sputter crater in the topography data. Otherwise, one has to rely on a known relation between image and erosion area thereby adding ambiguity, or at least more complexity, to the data analysis. The success of the registration process must be carefully examined by overlaying chemical and (registered) topography images in order to find a perfect match. This step is important as only slight registration errors may translate into huge depth scale calibration errors in cases where the sample exhibits strong topographical features (such as the trenches in the example of Figure 6.8).

Finally, as topography images typically provide only a relative change in surface height, the respective zero of all topography images must be shifted such that the average height of all pixels located outside the eroded crater area is the same. Then, subtraction of the images directly reveals the total depth that has been eroded during the entire depth profile as a function of the lateral pixel coordinate.

For the example of Figure 6.8, the resulting topography data are shown in Figure 6.17. If the erosion rates were identical at each pixel, the contour plot in Figure 6.17 would consist of only a single color. Clearly, the data show that this assumption is incorrect for the example presented here. Depending on the lateral position inside the crater, the total eroded depth spans a range of +300 to −50 nm, where negative values indicate the *buildup* instead of removal of material during ion bombardment. This finding is of central importance in converting a pseudo-3D image to a true three-dimensional representation as it indicates that the depth scale calibration must be performed *individually* on each lateral pixel of the analyzed area.

For the example presented here (Figure 6.17), analysis shows that the large lateral variation of the erosion rate is related to the chemical damage and gallium implantation produced by the FIB beam in connection with the large topography of the sample before the depth profile analysis. In particular, the dark blue or black colored patches inside the letters "PSU" indicate that the bottom of the FIB-eroded trenches *rises up* in the course of the depth profile, indicating an apparent filling

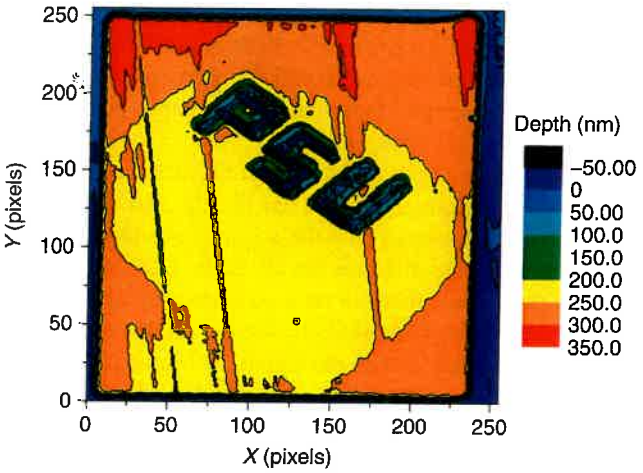


**Figure 6.17** Total eroded depth as a function of lateral pixel coordinate for the image depth profile depicted in Figure 6.8. Reproduced from Wucher et al.,[58] with permission from ACS Publications.

of the trench holes under $C_{60}^+$ bombardment which is caused by redeposition of material sputtered from the trench walls. It is interesting to note that this phenomenon occurs although the trench walls are actually not very steep,[¶] forming a maximum slope of less than 5° with respect to the original film surface. It can therefore be expected that effects similar to this will often play a role on samples featuring aspect ratios of that order or larger. In the regions showing a net buildup of material instead of removal, the depth scale is obviously ill-defined. In the remaining part of the crater, total erosion depths between 0 and 300 nm are observed.

As discussed earlier, the most direct approach to calculate the pixel-dependent erosion rate is to divide the total eroded depth at each pixel by the total projectile ion fluence. Assuming this average erosion rate to be constant throughout the depth profile, this would result in a constant (but pixel-dependent) height step between subsequent images (provided the chemical images are separated by equivalent fluence erosion cycles). The assumption of a constant erosion rate, on the other hand, is questionable when profiling across a vertical sequence of different layers and therefore also needs to be examined. For that purpose, it is advantageous to extract "regional" depth profiles from the acquired data set. These are obtained by summing the intensity of a particular measured mass spectrometric signal over all pixels within a selected area (region) of interest and plotting the result as a function of erosion time or projectile ion fluence. The selection of suitable regions depends on the nature of the investigated sample and therefore cannot be generalized. For the example of Figure 6.8, two different regions can be identified, namely (1) the area where the virgin molecular film is still present and (2) the area where the original

[¶]The steepness generally appears very exaggerated in AFM images because of the largely different vertical and lateral length scales.

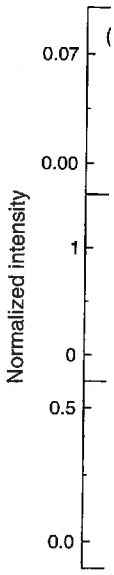


Figure 6.1
signals (arl
(red), and
pristine un
Ga-damag
Publicatior

surface w
respective
The
molecular
to comple
total erod
the calcul
between t
this can b

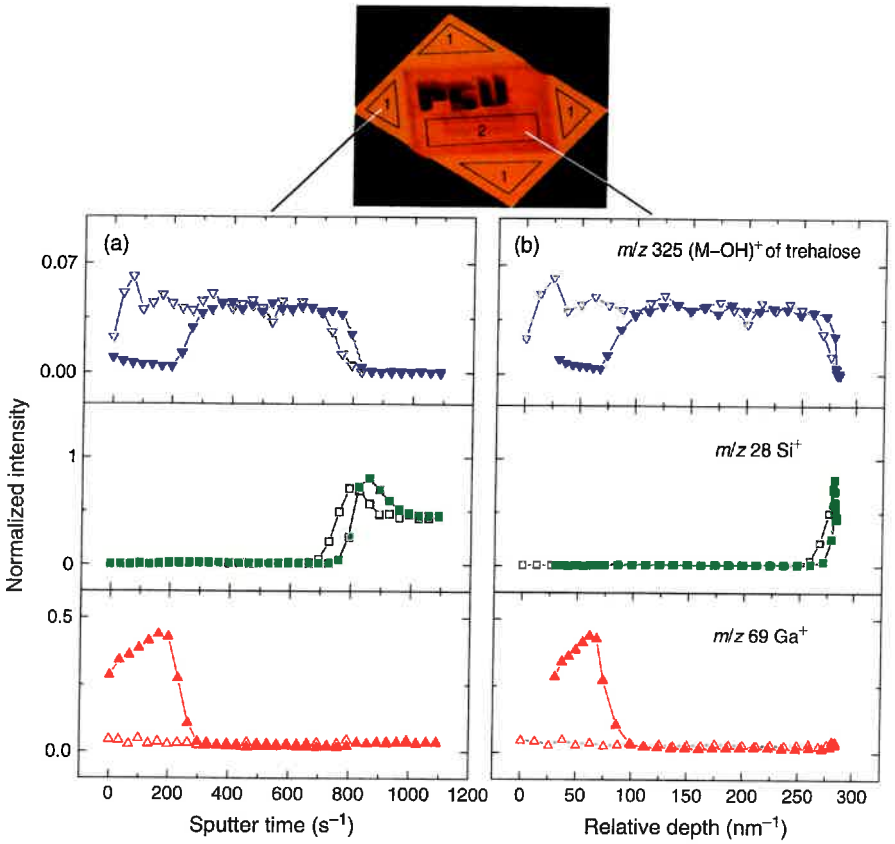


**Figure 6.18** Regional depth profiles extracted from the data of Figure 6.8. The plotted signals (arbitrary units) represent the intact molecular film (blue), the implanted gallium (red), and the silicon substrate (green). Open symbols represent the depth profile from the pristine undamaged region, while the closed symbols represent the depth profiles from the Ga-damaged regions. Recreated from Wucher et al.,[58] with permission from ACS Publications.

surface was subjected to $Ga^+$ ion prebombardment. For illustration purposes, the respective profiles are shown in Figure 6.18.

The data obtained for region (1) depicted in Figure 6.18a represent a typical molecular depth profile as described in detail in Chapter 5. From the fluence needed to completely remove the entire molecular film in connection with the measured total eroded depth; one can calculate the erosion rate of the undisturbed film. In the calculation, it must be taken into account that the erosion rate varies strongly between the molecular overlayer and the substrate. As a first order approximation,[55] this can be done by interpolation in the interface region according to

$$\dot{z} = \chi_{\text{film}} \cdot \dot{z}_{\text{film}} + \chi_{\text{substrate}} \cdot \dot{z}_{\text{substrate}} \tag{6.3}$$

where $\dot{z}_{\text{film}}$ and $\dot{z}_{\text{substrate}}$ denote the erosion rates of the molecular film and the substrate, respectively. The weighing factors $\chi_X$ must, in some way, be derived from the measured mass spectrometric signals. Various recipes have been published in the literature.[55–61] The most straightforward approach is to use a linear interpolation according to

$$\chi_X = \frac{I_X/I_X^{\max}}{\sum_Y I_Y/I_Y^{\max}} \quad (X, Y = \text{film, substrate}) \tag{6.4}$$

where $I_{\text{film}}^{\max}$ and $I_{\text{substrate}}^{\max}$ denote the respective maximum signal detected throughout the depth profile. The advantage of Equation 6.4 is that it automatically ensures the normalization $\sum_i \chi_i = 1$ and is easily extended to more than one interface (i.e., more than two significant signals). Using a known (measured) substrate erosion rate, the value of $\dot{z}_{\text{film}}$ can then be determined by integrating Equation 6.3 and equating the result with the measured total eroded depth.

In region (2) depicted in Figure 6.18b, the depth scale calibration is more complicated. At the beginning of the profile, erosion proceeds through the FIB-prebombarded material that is apparently heavily doped with gallium. In this regime, the molecular ion signals from the film are very low, indicating severe chemical damage induced by the $Ga^+$ impact. Both factors lead to an altered erosion rate when compared to the undisturbed film. After application of a certain ion fluence, on the other hand, the Ga signal disappears and the molecular ion signals rise to the same level as in the undisturbed film. In this regime, the undamaged film underneath the altered layer has been uncovered and is being removed with the same erosion rate as in region (1), until the substrate is reached. An essential, but so far unknown, quantity is the erosion rate within the Ga-doped/damaged layer. Using the same interpolation scheme as depicted in Equations 6.3 and 6.4, we can now write the erosion rate as

$$\dot{z} = \chi_{\text{Ga}} \cdot \dot{z}_{\text{altered layer}} + \chi_{\text{film}} \cdot \dot{z}_{\text{film}} + \chi_{\text{substrate}} \cdot \dot{z}_{\text{substrate}} \tag{6.5}$$

Inserting $\dot{z}_{\text{film}}$ and $\dot{z}_{\text{substrate}}$ from Equation 6.3, it is now possible to integrate Equation 6.5, set the result equal to the measured total eroded depth in this area, and solve for $\dot{z}_{\text{altered layer}}$. For the specific example of Figure 6.8, one finds a substantially reduced erosion rate across the damaged layer, which is only about 1/3 of that measured in the undisturbed film. In the silicon substrate, the erosion rate is by a factor of 37 smaller than in the intact molecular film. These findings illustrate the importance of an appropriate depth scale calibration that is determined by integrating Equation 6.5 as a function of sputter time or fluence. In the example of Figure 6.8, the thickness of the altered layer can be calculated to be about 50 nm.

We reiterate that the linear interpolation of erosion rates according to Equation 6.4 naturally represents only a first order approximation that may not be accurate in all cases, particularly for interfaces between layers with widely different sputter yields (e.g., a molecular film and an inorganic substrate). This approach is further questionable[62] in cases where intermediate layers (for instance oxide or hydroxide layers) are present at such an interface.[61] Moreover, it has been demonstrated that erosion rates induced by, for instance, a fullerene

cluster ion beam may drop with increasing eroded depth even if a homogeneous sample is being bombarded. The exact reason for this effect, which appears to be significantly reduced at low temperature[36,59,63] or if the erosion is performed with a rare gas cluster ion beam,[64] is currently not well understood. Certainly, the damage mechanisms described in Chapter 5 play a role. Therefore, it is of utmost importance to measure the erosion rate as a function of eroded depth. In lieu of an *in situ* measurement, this has to be done in an extremely time- and sample-intensive way by applying many different ion fluences and measuring the resulting erosion craters *ex situ*. Experiments of this kind have been conducted,[54,65,66] but it appears difficult to resolve the erosion rate variation across the shallow interface in this manner.[54]

An elegant strategy to obtain more detailed information is to erode a wedge-shaped crater by applying a linearly increasing fluence between both sides of the erosion area as was discussed earlier. In this way, one single topography measurement of the resulting crater is sufficient to determine (i) the nonlinear relation between fluence and erosion rates (from the slope of the wedge) and (ii) the fluence-dependent evolution of surface roughness under prolonged ion bombardment (from the high frequency "noise" of the wedge surface).[35] In principle, the wedge erosion can be interrupted at regular intervals and images can be taken at each step. After the topography measurement of the wedged crater, the sample can be reinserted and the same procedure can be applied in the opposite direction, thereby now eroding the wedge down to the substrate. The resulting image stack represents a set of tomographic slices in different directions, which can afterwards be converted into a true 3D representation of the eroded sample volume.

## 6.4 THREE-DIMENSIONAL IMAGE RECONSTRUCTION

In order to reconstruct the true three-dimensional structure of the analyzed sample, the location $(x, y, z)$ of each voxel $(i, j, k)$ of the data set needs to be calculated. Determination of $x$ and $y$ from the pixel indices $(j)$ and $(k)$ is straightforward, as the pixel steps $\Delta x$ and $\Delta y$ are easily calculated from the total number of pixels and the measured lateral dimensions of the sputter crater. Since the correlation between $(x, y)$ and $(j, k)$ remains constant—at least to first order—throughout the entire depth profile, this mapping only needs to be done once. The problematic part is the correlation between the vertical coordinate $(z)$ and the image index $(i)$ (denoting the first, second, third, etc. acquired images per sputter cycle), which will be different for each pixel $(j, k)$. In order to calculate $z(i, j, k)$, the nonlinear depth scale calibration described in Section 6.3 must be employed for each pixel of the lateral image area separately. In cases where different substructures are crossed in the vertical direction, signals representative for the specific chemistry of these structures must be identified and utilized for the erosion rate interpolation procedure. It is important to note that this process is highly sample specific and must be optimized separately for each individual system. It is this fact that renders true 3D imaging so hard to generalize, and it is also the reason why practically all published data on 3D sputter depth profiling have only been visualized in the

pseudo-3D mode (in some cases with substrate level correction as described in the following paragraphs).

We will illustrate the process again using the example of Figure 6.8. Starting from the original topography measurement, we define $z(i = 1, j, k)$ for the first image taken before sputter erosion begins. In principle, the depth interval $\Delta z$ eroded in each subsequent sputtering cycle must be calculated by interpolating the erosion rate between the values appropriate for the undisturbed molecular film, the altered layer, and the substrate, respectively, based on the respective mass spectral signals recorded in the previous image. Here, a problem arises because of the small number of secondary ions detected on each pixel, which makes a proper interpolation difficult. Hence, it will, in most cases, be necessary to sum (and average) the signal over a few neighboring pixels. The averaging process, however, results in a loss of lateral resolution which might lead to erroneous results in cases where erosion rates change drastically as a function of lateral image position. Such a situation may, for instance, occur if the substrate is reached in specific areas, while other neighboring areas still consist of molecular film material. In the specific example discussed here, we summed the signal over an area of $5 \times 5$ pixels and still found the resulting averaged signal too noisy for an interpolation scheme. In these cases, it might be better to *switch* instead of *interpolate* the erosion rate based on a threshold value of the averaged signals. In the particular example of the data presented in Figure 6.8, the erosion rates were therefore assumed to switch between the values of the altered layer and the intact molecular film if the averaged Ga signal exceeded a threshold value of 0.2 counts/pixel, and between the values of the molecular film and the substrate if the averaged Si signal exceeded a threshold value of 0.2 counts/pixel, respectively. The choice of the switching threshold is critical and needs to be optimized for each sample. The resulting three-dimensional representation of the data is depicted in Figure 6.19. In order to generate the displayed isosurface rendering, the irregularly spaced $(x, y, z, I)$ [‖] data need to be converted into an isospaced grid. For that purpose, the data set is first scanned to find the limiting values of the coordinates $x, y$, and $z$. While this is straightforward for $x$ and $y$ (with $x_{min}, y_{min}$ and $x_{max}, y_{max}$ corresponding to the lateral image area), the limits $z_{min}$ and $z_{max}$ depend on the measured surface topography. Then, a three-dimensional cell grid is spanned between these limits with a predefined cell dimension $\Delta x \times \Delta y \times \Delta z$. While $\Delta x$ and $\Delta y$ are naturally defined by the image pixel size, the value of $\Delta z$ can be arbitrarily set. As the next step, the $(x, y, z, I)$ data are binned into the cell grid by summing the intensity of all data points whose coordinates $(x, y, z)$ fall within a particular cell. Owing to the irregular nature of the measured data set (induced by the fact that the sample surface and therefore the image slices are not flat), there are many cells that contain no data point at all. In other words, these cells do not belong to the analyzed sample, as no point of the sample volume probed by the depth profile has coordinates $(x, y, z)$ that fall into such a cell. These cells therefore need to be distinguished from those that do contain data points (in other words, belong to the sample), albeit

[‖]Note that $I$ denotes the intensity of a particular mass spectrometric signal, and therefore there are as many such data sets as there are mass peaks of interest.

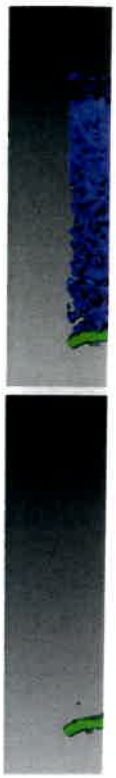

Figure 6.1
the data pr
Springer.

with zero
intensity
means of
interval v
combine
using thr
supercell.
depth acr
$Ga^+$ preb
At
face imag
play an e
faces cor
threshold
alization
sense if t
lower tha

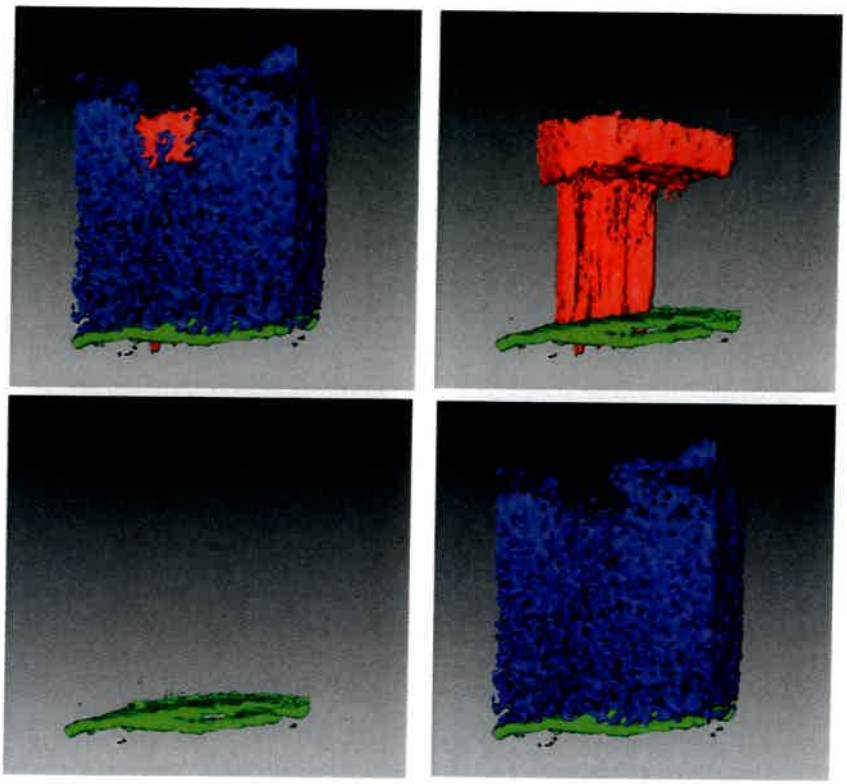

**Figure 6.19** Three-dimensional sample reconstruction with corrections, calculated from the data presented in Figure 6.8. Reproduced from Wucher et al.,[75] with permission from Springer.

with zero signal intensity, $I$. For that purpose, these cells were given a negative intensity value in order to be able to exclude them from the rendering process by means of a filter. For the visualization displayed in Figure 6.19, the depth sampling interval was set as $\Delta z = 1$ nm and the resulting cell array was downsampled to combine $5 \times 5 \times 5$ cells into one supercell. Isosurface rendering was performed using threshold intensity values of 25 (Ga), 20 (Si), and 1 (peptide) counts per supercell. It is seen that the substrate is now reached at approximately the correct depth across the entire crater. Moreover, the thickness of the altered layer in the $Ga^+$ prebombarded area is consistent with the depth profile data of Figure 6.18b.

At this point, a few words are in order regarding the interpretation of isosurface images. It should be noted that the threshold values used in such a visualization play an extremely important role as the displayed features represent contour surfaces connecting points where the respective signal closely approximates these threshold values. Changing these values may therefore drastically change the visualization result. From a fundamental perspective, the rendering process only makes sense if there is a clear separation between regions with signal that is higher or lower than the selected threshold value. If there is a connected volume of high

signal surrounded by a volume with low signal, then the result of the rendering process will be a closed surface, showing the contour of the high signal region. This is visible for the red and green surfaces displayed in Figure 6.19, which separate the gallium-implanted sample volume (red) and the silicon substrate (green) from the intact molecular film volume. In this case, the spatial extension of the displayed feature depends on the threshold value and will shrink and expand with increasing or decreasing threshold, respectively. If the threshold is lowered down to the noise level of the signal, the rendered isosurface will disintegrate into many little features. This is visible for the blue surface that basically separates volumes with any peptide intensity from those with zero intensity. In this case, the rendered image displays a volumetrically filled region, where the definition of an isosurface becomes meaningless. Nevertheless, the resulting image is still usable here to visualize the volume of the intact molecular film.

In order to better visualize the data, each secondary ion image can be superimposed with the corresponding surface topography and displayed separately. In this way, the entire depth profile can be viewed as a series of sequential three-dimensional images illustrating the development of the topography along with the chemical composition at the momentary surface. For the example of Figure 6.19, snapshots at particularly interesting points of the profile are shown in Figure 6.20. It is seen that the first image displays the original surface topography locating the gallium signal (red) inside the FIB-eroded crater and within the deep trenches, respectively. During the evolution of the profile, it is evident that the virgin trehalose (blue) overlayer is more rapidly removed than the $Ga^+$-altered layer, resulting in a rather flat surface after the altered layer has been removed. While the remaining overlayer is quickly eroded in the regions away from the trenches, no change in height is observed at some points inside the walls of the original trenches. At the bottom of the deep trenches, the surface is seen to move upward as depth profiling proceeds.

The three-dimensional data set produced using the above procedures is still not free from artifacts. This is due to the fact that a surface topography measurement using techniques such as AFM employs correction procedures that level the average height across an acquired image. As a consequence, any large-scale gradient of the surface height will automatically be leveled. In order to illustrate the consequence of this problem, a cross-sectional view of the data set presented in Figure 6.19 is shown in Figure 6.21. It is seen that the data indicate a slope of the film–silicon interface, which must clearly be wrong as it is known that the substrate surface is flat. In principle, such information must be utilized by applying another correction to the data set, which renders the film–substrate interface horizontal. For that purpose, the index $i_{\text{switch}}$ is identified for each pixel stack $(j,k)$ where the erosion rate is switched from the film to the substrate value. Then, all $z$ values of this pixel stack are shifted in parallel in order to render $z(i_{\text{switch}})$ at the same height. Note that this "leveling correction" (which is the same as that published by Breitenstein et al.[67–69] and applied to the data presented in Figure 6.5[70] and Figure 6.26[71]) requires prior knowledge about the sample and is therefore not easily generalized.

What can be deduced from Figure 6.21 is that the thickness of the molecular film deposited on the substrate must vary across the analyzed lateral area by as

Figure 6.2
presented ir
with permis

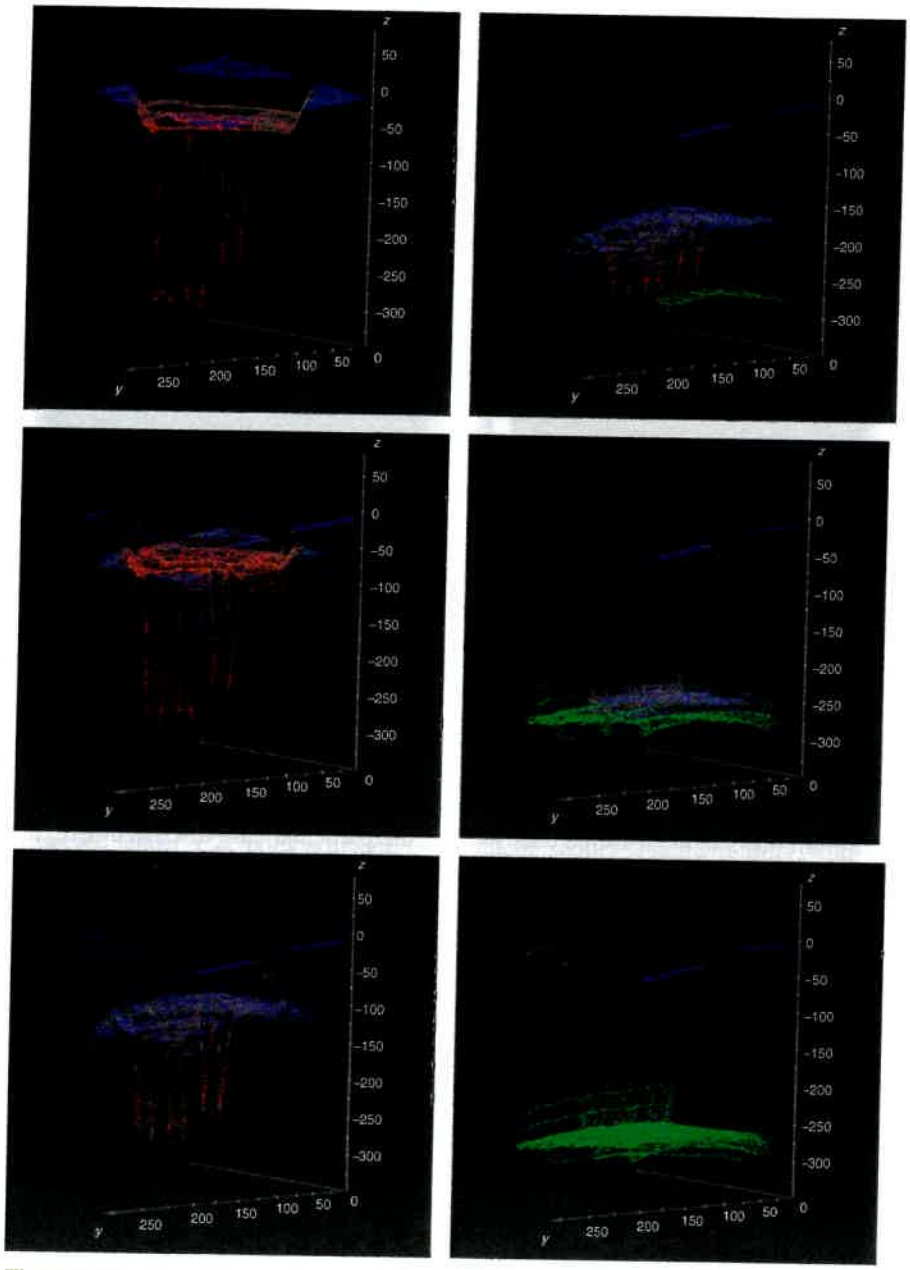


**Figure 6.20** Three-dimensional visualization of selected SIMS images from the data set presented in Figure 6.8 overlayed with topography. Reproduced from Wucher et al.,[58] with permission from ACS Publications.

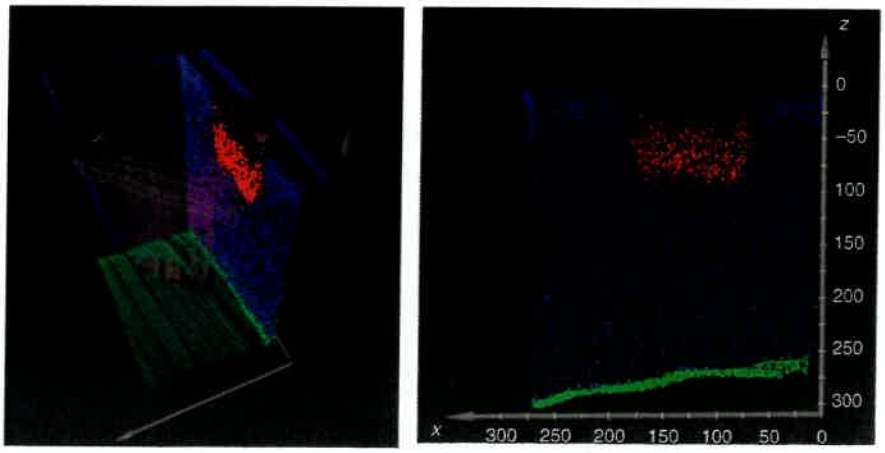


**Figure 6.21** Vertical cross-sectional view of the data set presented in Figure 6.8.[58] Figure reprinted from Wucher et al.,[75] with permission from Springer.

much as 10% of the entire film thickness (~30 nm in this case). This finding has important consequences with respect to the apparent depth resolution in sputter depth profiling experiments. From Figure 6.21, it is entirely clear that a sputter depth profile acquired with a gating area of about half the sputter crater dimension must necessarily exhibit an artificial interface width contribution of about 20 nm which arises exclusively from large-scale film thickness fluctuations. In order to investigate and eliminate such effects, three-dimensional depth profiling data is extremely helpful, as regional depth profiles can be extracted with different gating area from one single measured data set. For the particular case discussed here, the apparent depth resolution was found to improve significantly with decreasing gating area as shown in Figure 6.22.[72] By extrapolating the resulting data to zero area, the "intrinsic" depth resolution can be determined as an important characteristic of the depth profiling method (~7 nm in the present case[72]).

## 6.5 DAMAGE AND ALTERED LAYER DEPTH

On the basis of the concepts described above, one can investigate the influence of a FIB ion beam on a molecular film in more detail. Of particular interest are the following questions:

1. How does the altered (damaged) layer evolve as a function of accumulated ion fluence?
2. Does a polyatomic ion, for instance, $Au_3^+$, generate less damage than a monatomic ($Au^+$ or $Ga^+$) beam?

In order to address the first question, we refer to an experiment similar to that described in the previous section. In this case, a Langmuir–Blodgett (LB) multilayer film of 400 nm thickness deposited on a silicon substrate was

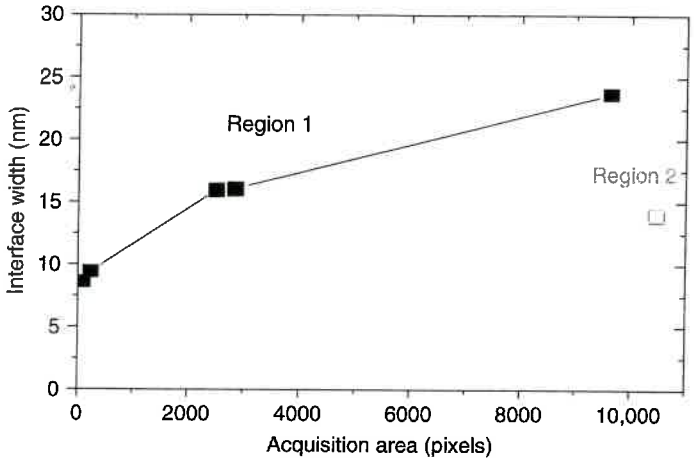


**Figure 6.22** Interface width determined from selected pixels within the imaged area of the data presented in Figure 6.8 versus "gating area" selected for the analysis. Reproduced from Wucher et al.,[72] with permission from Elsevier.

prebombarded with 15 keV $Au^+$, $Au_2^+$, and $Au_3^+$ ion beams to varying fluences and subsequently analyzed in a 3D depth profile using a 40 keV $C_{60}^+$ ion beam for sputtering and image acquisition.[73] Interestingly, even under prolonged bombardment with the gold beam (up to fluences of several $10^{15}$ ions/cm$^2$) the sample could not be eroded to more than a depth of about 15 nm. It is presently unclear what causes this effect; possible explanations could include charging or a beam chemistry-induced quenching of the erosion rate similar to that sometimes observed under $C_{60}$ bombardment. Subsequent sputter depth profiling with the $C_{60}^+$ beam revealed a severely damaged subsurface region at the gold-bombarded part of the surface. The surface topography within the image area before and after acquisition of the 3D depth profile is shown in Figure 6.23. As a technical side note, the figure shows that the data had to be subjected to a special smoothing algorithm in order to remove spikes originating from dust particles which would otherwise corrupt the depth scale calibration. The data show that significant surface topography evolves during erosion of the gold prebombarded area, while this is not the case in regions where the virgin molecular film is being removed. It is also observed that the erosion rate of the damaged subsurface layer must be smaller than that of the intact film. The three-dimensional reconstruction of the sample along with a 3D visualization of selected image frames is shown in Figures 6.24 and 6.25, respectively. A strongly enhanced signal of $C^+$ and $C_2^+$ secondary fragment ions can be found in the altered subsurface layer, which is visualized by the red isosurface in Figure 6.24. At the same time, the molecular ion signal of the intact LB film (blue) is practically absent in this volume, indicating almost complete fragmentation of the molecular film within the altered layer influenced by the gold prebombardment. Again, one finds a significantly reduced erosion rate when profiling across the altered layer as compared to the intact molecular film, indicating that this might be a general feature of cluster beam molecular depth profiling.

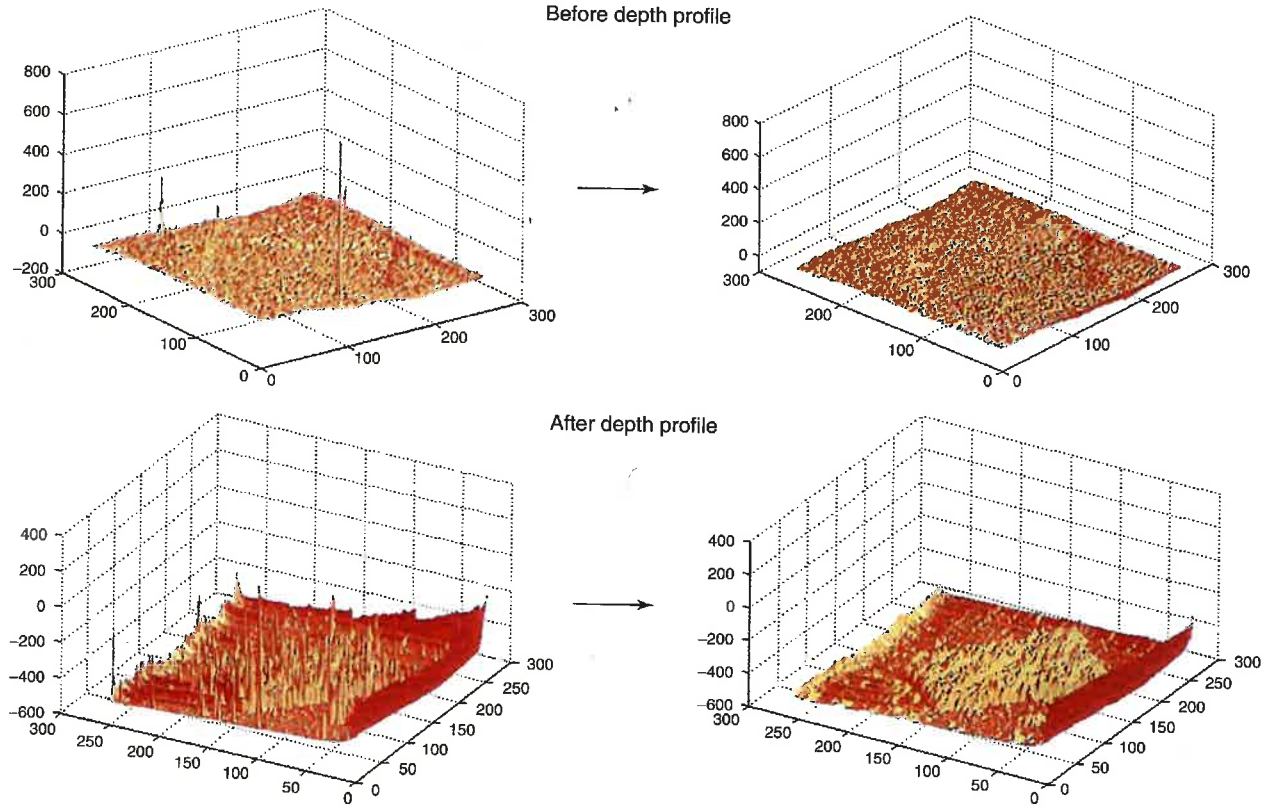


Figure 6.23 AFM images (vertical axis in nm, horizontal axes in μm) of the sputtered crater bottom taken before and after a 3D sputter depth profile of a 300 nm Langmuir–Blodgett molecular film on silicon. The sample was prebombarded with an LMIG $Au^+$ ion beam in the central area visible in the images. Left panels: data before smoothing; right panels: data after smoothing. Data courtesy of Lu et al.[73]

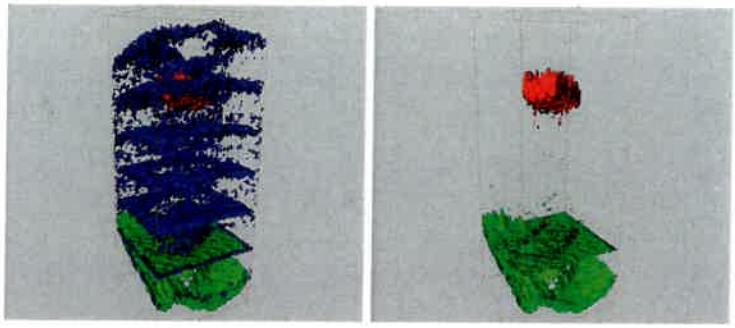


**Figure 6.24** Three-dimensional reconstruction of a Langmuir–Blodgett molecular film composed of 400 nm lipid film deposited on a silicon substrate which was prebombarded with a 15 keV $Au^+$ ion beam. The profile was acquired using a 40 keV $C_{60}^+$ cluster ion beam for sputtering and image acquisition. Data courtesy of Lu et al.[73] Green = Si substrate, blue = arachidic acid (AA) molecular signal, and red = carbon fragments.

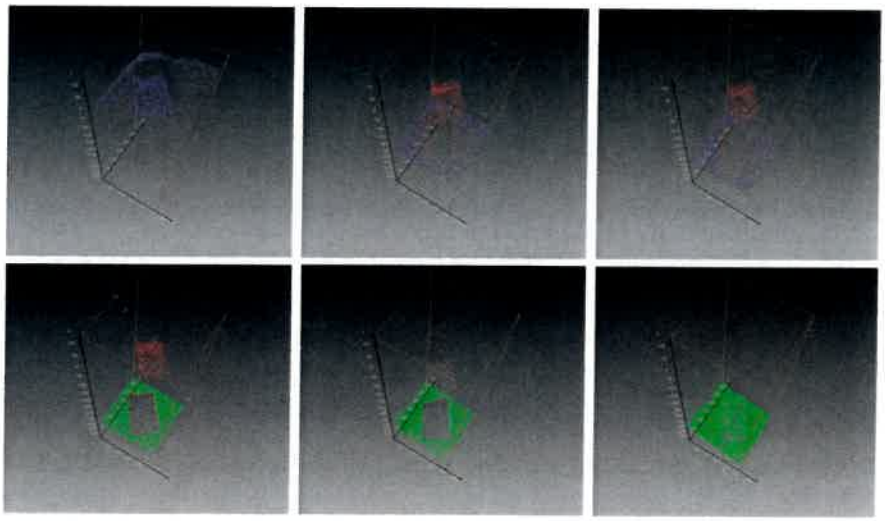

**Figure 6.25** Three-dimensional visualization of selected SIMS images from the data set presented in Figure 6.24 overlayed with topography. Data courtesy of Lu et al.[73]

Using the same procedures as described above, one can determine the thickness of the altered layer as a function of the gold projectile ion fluence (C. Lu, A. Wucher and N. Winograd, unpublished data). The altered layer thickness is found to increase with increasing gold ion fluence even when sputter erosion has already stopped, reaching a steady-state value of about 100 nm after impact of about $6 \times 10^{14}$ $Au^+$ ions/cm$^2$. This value is even larger than the one determined for a 15 keV $Ga^+$ bombardment of trehalose (50 nm), a finding that might be due to a larger penetration depth of the heavier gold projectile and/or the ordered structure

**Figure 6.23** AFM images (vertical axis in nm, horizontal axes in μm) of the sputtered crater bottom taken before and after a 3D sputter depth profile of a 300 nm Langmuir–Blodgett molecular film on silicon. The sample was prebombarded with an LMIG $Au^+$ ion beam in the central area visible in the images. Left panels: data before smoothing; right panels: data after smoothing. Data courtesy of Lu et al.[73]

of the LB multilayer film. In any case, the data confirm that damaged layer thicknesses of several ten nanometers coming out as fit parameters of the erosion dynamics model (see Chapter 5) are probably realistic. From the perspective of the FIB-ToF method, the data indicate that the best ion beam milling conditions, in terms of altered layer thickness (i.e., straggle) and the cleanup/polishing requirements, may be achieved with the use of the lower mass Ga ion.

In regards to the second question, while the altered layer thickness decreases with increasing nuclearity, this may not necessarily translate to more ideal FIB-SIMS etching. Simulation data for $Au_3^+$ and $Au^+$ sputtering, for example, shows that the lateral component of damage is greater for $Au_3^+$ than for $Au^+$. This is because Au has only a single trajectory, while the $Au_3^+$ breaks up into three divergent trajectories. Thus, in the case of FIB-ToF, in which vertical slicing is performed, it is likely that more polishing may be required to remove the lateral component of the beam-induced damage caused by $Au_3^+$ than for $Au^+$. Thus far there have not been any studies to verify this hypothesis.

## 6.6 BIOLOGICAL SAMPLES

In many biological applications, samples need to be kept at cryogenic temperatures during the entire analysis. While this is no problem with regard to the sputter depth profile (commercially available ToF-SIMS instrumentation is capable of handling and analyzing frozen samples), it poses a significant problem for the determination of surface topography. The protocol described is therefore likely to be impractical on samples such as, for instance, frozen-hydrated cells. Although there is commercially available instrumentation for low temperature AFM, these instruments usually have a very restricted maximum field-of-view (of the order of 10 μm) which is too small to capture an image of the entire sputter crater. Since we are not aware of commercially available optical interferometry instrumentation with nanometer height resolution that would be compatible with cryogenic sample cooling, measurement of the surface topography appears problematic and the depth scale calibration described in Section 6.3 cannot easily be performed for this type of sample. Therefore, the data treatment in most of the work published in this field is restricted to the assumption of a constant erosion rate across the entire eroded volume. Although this assumption is prone to fail when profiling across largely different matrices, one might argue that frozen-hydrated samples mostly consist of water ice as the main matrix material, thus rendering the assumption of a constant erosion rate not too far-fetched. Note, however, that this argument fails if the sample exhibits steep topographical features with large angle slopes. In order to still arrive at a meaningful three-dimensional reconstruction of the analyzed volume, one can determine the erosion rate from the ion fluence needed to remove a water ice film of known thickness (deposited, for instance, by dosing water vapor into the vacuum system). Then, utilizing the condition that the substrate is known to be flat, it is possible to use the leveling correction by rescaling the height coordinate based on the appearance of substrate related signals in the mass spectrum. An example of such an analysis is shown in Figure 6.26, where single HeLa cells deposited

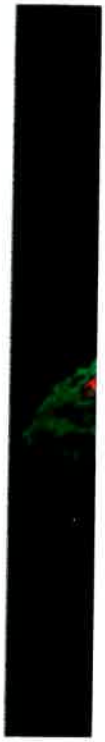

Figure 6
phosphoc
HeLa-M

on a stai
$C_{60}^+$ ior
to recon
nuclei fa
renderin
instance.
threshol

6.7 C

High res
still pos
focusabl
spectron
ble to er
integrity
profiling

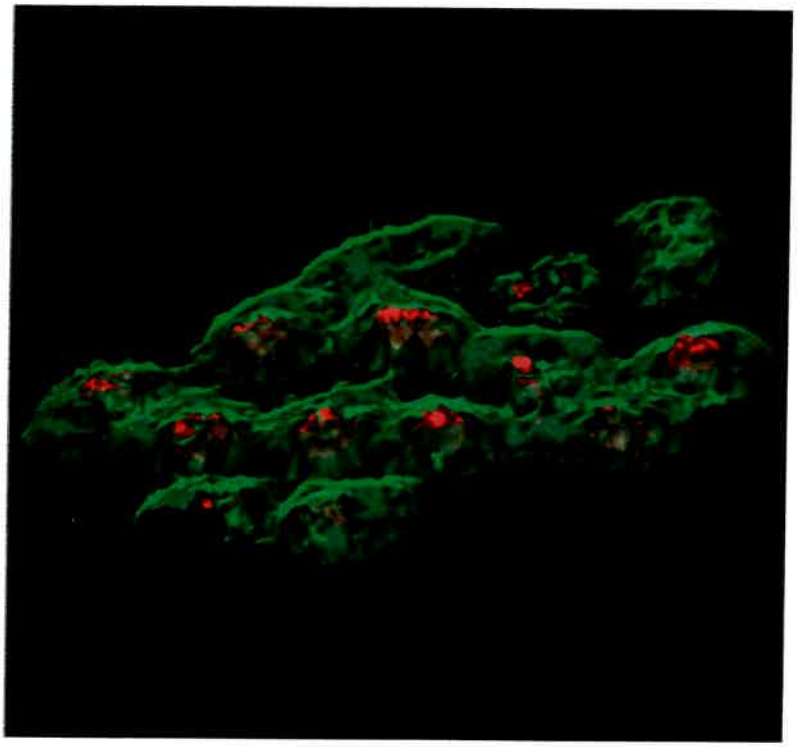

Figure 6.26 Three-dimensional visualization of the membrane (green, *m/z* 184.1, phosphocholine) and nucleus (red, *m/z* 136.1, adenine) chemistry in frozen-hydrated HeLa-M cells. Reproduced from Fletcher et al.[71] with permission from Wiley.

on a stainless steel substrate were subjected to a 3D depth profile using a 40 keV $C_{60}^+$ ion beam. It is seen that the analysis of specific molecular signals allows one to reconstruct the shape of the cell membrane as well as the location of the cell nuclei fairly well. It should be noted again, however, that the chosen isosurface rendering does not easily permit a quantitative estimate of the dimension of, for instance, the cell nucleus without a thorough investigation of the role of the used threshold value.

## 6.7 CONCLUSIONS

High resolution three-dimensional chemical characterization at the molecular level still poses a significant challenge in surface and thin-film analysis. The advent of focusable cluster ion beams has greatly enhanced the capabilities of surface mass spectrometry in this field. Using cluster ion beams such as $C_{60}^+$ or $Ar_n^+$, it is possible to erode molecular surfaces by ion sputtering without destroying the molecular integrity of the sample. As a consequence, techniques such as imaging sputter depth profiling or FIB-ToF tomography can now be extended to molecular structures as

well, thereby opening up new application fields such as organic semiconductors, polymer chemistry, and biology. Using LMIGs providing cluster ion beams such as $Au_n^+$ and $Bi_n^+$, the lateral resolution of such an analysis can be pushed to the submicrometer level allowing, in principle, for a spatial resolution on the order of 100 nm. However, one must keep in mind that the useful resolution is often limited by detection sensitivity. Moreover, care needs to be taken when converting measured data into true 3D information about the analyzed structure. While simple image stacking may in some cases be a reasonable approximation, effects such as differential sputtering may in other cases cause severe distortions of the measured profiles. These effects must therefore be examined for every projectile/sample combination and corrected, in order to arrive at a reasonable 3D representation of the analyzed sample volume.

## REFERENCES


1. Chabala, J. M.; Levi-Setti, R.; Wang, Y. L. *Appl. Surf. Sci.* **1988**, 32 (1–2), 10–32.
2. Levi-Setti, R.; Wang, Y. L.; Crow, G. *Appl. Surf. Sci.* **1986**, 26 (3), 249–264.
3. Levi-Setti, R.; Chabala, J. M.; Hallegot, P.; Yuh, L. W. *Microelectron. Reliab.* **1989**, 9 (1–4), 391–399.
4. Levi-Setti, R., Hallegot, P., Girod, C., Chabala, J. M., Li, J., Sodonis, A., and Wolbach, W. *Surf. Sci.* **1991**, 246 (1–3), 94.
5. Chabala, J. M.; Levi-Setti, R.; Wang, Y. L. *J. Vac. Sci. Technol.* **1988**, 6 (3), 910–914.
6. Levi-Setti, R.; Chabala, J. M.; Wang, Y. L. *Ultramicroscopy* **1988**, 24 (2–3), 97–113.
7. Levi-Setti, R., Chabala, J., and Wang, Y. L. *Scanning Microsc.* **1987**, 1 (1), 13–22.
8. Hallegot, P., Girod, C., Le Beau, M. M.; Levi-Setti, R. *Int. Soc. Opt. Eng.* **1991**, 1396, 311–315.
9. Hindie, E., Hallegot, P., Chabala, J. M., Thorne, N. A., Coulomb, B., Levi-Setti, R.; Galle, P. *Scanning Microsc.* **1988**, 2 (4), 1821–1829.
10. Pumphrey, G. M.; Hanson, B. T.; Chandra, S.; Madsen, E. L. *Environ. Microbiol.* **2009**, 11 (1), 220–229.
11. Chandra, S.; Pumphrey, G.; Abraham, J. M.; Madsen, E. L. *Appl. Surf. Sci.* **2008**, 255 (4), 847–851.
12. Chandra, S. *Appl. Surf. Sci.* **2004**, 231, 467–469
13. Chandra, S. *Appl. Surf. Sci.* **2003**, 203, 679–683.
14. Chandra, S.; Smith, D. R.; Morrison, G. H. *Anal. Chem.* **2000**, 72 (3), 104A–114A.
15. Fahey, A., Gillen, G., Chi, P.; Mahoney, C. *Appl. Surf. Sci.* **2006**, 252, 7312–7314.
16. Gillen, G.; Batteas, J.; Michaels, C. A.; Chi, P.; Small, J.; Windsor, E.; Fahey, A.; Verkouteren, J.; Kim, K. J. *Appl. Surf. Sci.* **2006**, 252 (19), 6521–6525.
17. Gillen, G.; Fahey, A. *Appl. Surf. Sci.* **2003**, 203–204, 209–213.
18. Gillen, G.; Roberson, S.; Fahey, A.; Walker, M.; Bennett, J.; Lareau, R. T. *AIP. Conf. Proc.* **2001**, 550, 687–691.
19. Gillen, G., Walker, M., Thompson, P., and Bennett, J. *J. Vac. Sci. Technol.* **2000**, 18 (1), 503–508.
20. Gillen, G.. Secondary Ion Mass Spectrometry Using Polyatomic and Cluster Primary Ion Beams. In Microbeam Analysis 2000; IOP publishing: Bristol, **2000**, pp. 339–340.
21. Gillen, G., Roberson, S., Ng, C.; Stranick, M. *Scanning* **1999**, 21 (3), 173–181.
22. Niehuis, E.; Grehl, T.; Kollmer, F.; Moellers, R.; Rading, D.; Kersting, R.; Hagenhoff, B. *Surf. Interface Anal.* **2011**, 43 (1–2), 204–206.
23. Gillen, G.; Fahey, A.; Wagner, M.; Mahoney, C. *Appl. Surf. Sci.* **2006**, 252 (19), 6537–6541.
24. Fisher, G. L.; Belu, A. M.; Mahoney, C. M.; Wormuth, K.; Sanada, N. *Anal. Chem.* **2009**, 81 (24), 9930–9940.
25. D. Rading et al., Data presented by IonToF GmbH at the Annual SIMS Workshop, Baltimore and the International SIMS conference, Riva del Garda, **2011**.

26. Fletcher, J. S.; Lockyer, N. P.; Vaidyanathan, S.; Vickerman, J. C. *Anal. Chem.* **2007**, 79 (6), 2199–2206.
27. Nygren, H.; Borner, K.; Malmberg, P.; Hagenhoff, B. *Appl. Surf. Sci.* **2006**, 252 (19), 6975–6981.
28. Carado, A.; Passarelli, M. K.; Kozole, J.; Wingate, J. E.; Winograd, N.; Loboda, A. V. *Anal. Chem.* **2008**, 80 (21), 7921–7929.
29. Hill, R.; Blenkinsopp, P.; Thompson, S.; Vickerman, J.; Fletcher, J. S. *Surf. Interface Anal.* **2011**, 43 (1–2), 506–509.
30. Fletcher, J. S.; Rabbani, S.; Henderson, A.; Blenkinsopp, P.; Thompson, S. P.; Lockyer, N. P.; Vickerman, J. C. *Anal. Chem.* **2008**, 80 (23), 9058–9064.
31. Thompson, D. A.; Johar, S. S. *Appl. Phys. Lett.* **1979**, 34 (5), 342–345.
32. Hsu, C. M.; McPhail D. S. *Nucl. Instrum. Meth.* **1995**, 101 (4), 427–434.
33. Skinner, D. K. *Surf. Interface Anal.* **1989**, 14 (9), 567–571.
34. Voigtmann, R.; Moldenhauer, W. *Surf. Interface Anal.* **1988**, 13 (2–3), 167–172.
35. Mao, D.; Wucher, A.; Winograd, N. *Anal. Chem.* **2010**, 82 (1), 57–60.
36. Mao, D.; Lu, C.; Winograd, N.; Wucher, A. *Anal. Chem.* **2011**, 83, 6410–6417.
37. Crecelius, A. C.; Cornett, D. S.; Caprioli, R. M.; Williams, B.; Dawant, B. M.; Bodenheimer, B. *J. Am. Soc. Mass Spectrom.* **2005**, 16 (7), 1093–1099.
38. Eberlin, L. S.; Ifa, D. R.; Wu, C.; Cooks, R. G. *Angew. Chem. Int. Ed.* **2010**, 49 (5), 873–876.
39. Hinder, S. J.; Lowe, C.; Maxted, J. T.; Watts, J. F. *Surf. Interface Anal.* **2004**, 36 (12), 1575–1581.
40. Holzer, L.; Indutnyi, F.; Gasser, P. H.; Munch, B.; Wegmann, M. *J. Microsc.* **2004**, 216 (1), 84–95.
41. Stevie, F. A.; Vartuli, C. B.; Giannuzzi, L. A.; Shofner, T. L.; Brown, S. R.; Rossie, B.; Hillion, F.; Mills, R. H.; Antonell, M.; Irwin, R. B. *Surf. Interface Anal.* **2001**, 31 (5), 345–351.
42. Heymann, J. A. W.; Hayles, M.; Gestmann, I.; Giannuzzi, L. A.; Lich, B.; Subramaniam, S. *J. Struct. Biol.* **2006**, 155 (1), 63–73.
43. Stevie, F. A.; Downey, S. W.; Brown, S. R.; Shofner, T. L.; Decker, M. A.; Dingle, T.; Christman, L. *J. Vac. Sci. Technol. B* **1999**, 17, 2476.
44. Giannuzzi, L. A.; Utlaut M. *Surf. Interface Anal.* **2011**, 43 (1–2), 475–478.
45. G. L., Fisher et al., Data presented at the Annual SIMS workshop, Norfolk, VA, 2010 and the International SIMS XVIII conference, Riva del Gorda, Italy, 2011.
46. Volkert, C. A.; Minor, A. M. *MRS Bull.* **2007**, 32 (05), 389–399.
47. Fisher, G. L.; Belu, A. M.; Mahoney, C. M.; Wormuth, K.; Sanada, N. *Anal. Chem.* **2009**, 81 (24), 9930–9940.
48. Volkert, C. A.; Minor, A. M. *MRS Bull.* **2007**, 32 (05), 389–399.
49. Prenitzer, B. I.; Urbanik-Shannon, C. A.; Giannuzzi, L. A.; Brown, S. R.; Irwin, R. B.; Shofner, T. L.; Stevie, F. A. *Microsc. Microanal.* **2003**, 9 (03), 216–236.
50. Mahoney, C. M.; Fahey, A. J.; Belu, A. M. *Anal. Chem.* **2008**, 80 (3), 624–632.
51. de Winter, D. A. M.; Mulders, J. J. L.. *Redeposition Characteristics of Focused Ion Beam Milling for Nanofabrication*; AVS, **2007**, pp. 2215–2218.
52. Bhavsar, S. N.; Aravindan, S.; Rao, P. V. *Precis. Eng.* **2012**, 36 (3), 408–413.
53. Fu, Y. Q.; Bryan, N. K. A.; Shing, O. N.; Hung, N. P. *Int. J. Adv. Manuf. Technol.* **2000**, 16 (12), 877–880.
54. Kozole, J., Wucher, A.; Winograd, N. *Anal. Chem.* **2008**, 80, 5293–5301.
55. Cheng, J.; Wucher, A.; Winograd, N. *J. Phys. Chem. B.* **2006**, 110 (16), 8329–8336.
56. Wagner, M. S. *Anal. Chem.* **2005**, 77 (3), 911–922.
57. Cheng, J.; Winograd, N. *Anal. Chem.* **2005**, 77 (11), 3651–3659.
58. Wucher, A., Cheng, J.; Winograd, N. *Anal. Chem.* **2007**, 79 (15), 5529–5539.
59. Zheng, L.; Wucher, A.; Winograd, N. *J. Am. Soc. Mass Spectrom.* **2008**, 19, 96–102.
60. Wucher, A.; Cheng, J.; Winograd, N. *Appl. Surf. Sci.* **2008**, 255 (4), 959–961.
61. Green, F. M.; Shard, A. G.; Gilmore, I. S.; Seah, M. P. *Anal. Chem.* **2009**, 81 (1), 75–79.
62. Mahoney, C. M. *Mass Spectrom. Rev.* **2010**, 29 (2), 247–293.
63. Lu, C.; Wucher, A.; Winograd, N. *Anal. Chem.* **2010**, 83 (1), 351–358.
64. Lee, J. L. S.; Ninomiya, S.; Matsuo, J.; Gilmore, I. S.; Seah, M. P.; Shard, A. G. *Anal. Chem.* **2010**, 82 (1), 98–105.
65. Shard, A. G.; Green, F. M.; Brewer, P. J.; Seah, M. P.; Gilmore, I. S *J. Phys. Chem. B.* **2008**, 112 (9), 2596–2605.

66. Shard, A. G.; Brewer, P. J.; Green, F. M.; Gilmore, I. S. *Surf. Interface Anal.* **2007**, 39 (4), 294–298.
67. Breitenstein, D.; Rommel, C. E.; Stolwijk, J.; Wegener, J.; Hagenhoff, B. *Appl. Surf. Sci.* **2008**, 255 (4), 1249–1256.
68. Breitenstein, D.; Rommel, C. E.; Mollers, R.; Wegener, J.; Hagenhoff, B. *Angew. Chem. Int. Ed.* **2007**, 46 (28), 5332–5335.
69. Breitenstein, D.; Batenburg, J. J.; Hagenhoff, B.; Galla, H. J. *Biophys. J.* **2006**, 91 (4), 1347–1356.
70. Fletcher, J. S.; Vickerman, J. C. *Anal. Bioanal. Chem.* **2010**, 396 (1), 85–104.
71. Fletcher, J. S.; Rabbani, S.; Henderson, A.; Lockyer, N. P.; Vickerman, J. C. *Rapid Commun. Mass Spectrom.* **2011**, 25 (7), 925–932.
72. Wucher, A.; Cheng, J.; Zheng, L. L.; Willingham, D.; Winograd, N. *Appl. Surf. Sci.* **2008**, 255 (4), 984–986.
73. Lu, C.; Wucher, A.; Winograd N. *Surf. Interface Anal.* **2012**, doi:10.1002/sia.4838.
74. Nygren, H.; Hagenhoff, B.; Malmberg, P.; Nilsson, M.; Richter, K. *Microsc. Res. Tech.* **2007**, 70 (11), 969–974.
75. Wucher, A.; Cheng, J.; Zheng, L.; Winograd N. *Anal. Bioanal. Chem.* **2009**, 393 (8), 1835–1842.